THE ASTROPHYSICAL JOURNAL, 443:35–53, 1995 April 10

THE PARSEC-SCALE JET IN QUASAR 3C 345

J. ANTON ZENSUS
National Radio Astronomy Observatory, 520 Edgemont Road, Charlottesville, VA 22903
AND
MARSHALL H. COHEN AND STEPHEN C. UNWIN
Owens Valley Radio Observatory, California Institute of Technology, Mail Code 105-24, Pasadena, CA 91125
Received 1994 May 23; accepted 1994 October 20

ABSTRACT

The quasar 3C 345 ($z = 0.6$) was monitored with very long baseline interferometry (VLBI) in 11 imaging observations at 5, 11, and 22 GHz during 1984.8–1988.2. The images probe detail of the superluminal radio jet over distances ranging from 0.12 to 12 mas (0.5–45 pc, for $H_0 = 100$ km s^{-1} Mpc^{-1}, $q_0 = 0.5$) from the unresolved radio "core." The structure of the VLBI jet is well described by two to four distinct components, but some of the images also indicate the presence of underlying jet emission, as seen in recent high dynamic range imaging.

The component motions are analyzed using polynomial fits to the position offsets $x(t)$ and $y(t)$ relative to the core, in a form suitable for comparison with three-dimensional jet models. Components C2–C5 show superluminal motion over the full jet length. The measured speeds increase monotonically with time (or distance from the core), from $\sim 3c$ to $\sim 10c$, consistent with a jet of constant Lorentz factor ($\gamma = 10$) bending away from the line of sight.

Near the core the jet ridge line, as traced by the superluminal features, is strongly curved. Trajectories of successive components differ substantially within 2 mas from the core, but they become parallel at larger distances. The outer components show monotonic curvature, but the path of feature C4 shows at least two changes in curvature, or "wiggles." We reconstruct the three-dimensional path of C4 and show that its modest intrinsic bend is amplified by projection effects: the path starts within $\sim 1°$ of the line of sight, and then bends smoothly away to $\sim 4°$, consistent with the observed straightening of the projection of the jet on the sky.

We present a model for the radio through X-ray emission from 3C 345 which self-consistently combines the inhomogeneous-jet model of Königl for the core with homogeneous spheres for the superluminal components. This (constant Lorentz factor) model accounts for the flat radio spectrum of the nucleus and the steep spectra of the superluminal components, as derived from the VLBI images, as well as for kinematic constraints from the proper motions. The best fit requires a small opening angle for the core of $\simeq 0°.5$, which, like the jet bending, is amplified by projection. Inverse Compton emission from the nucleus is the likely origin of the observed soft X-ray flux, and it probably dominates over X-rays from the superluminal components. To avoid overprediction of X-rays by the model, the jet axis must lie within 5°.4 of the line of sight, consistent with, but independent of, constraints from kinematics. The kinetic luminosity of the parsec-scale jet is sufficient to power the outer radio halo, but barely if the jet is light; we regard this as evidence in favor of a heavy jet; i.e., the dynamics are proton dominated.

Subject headings: galaxies: jets — quasars: individual (3C 345) — radiation mechanisms: nonthermal — radio continuum: galaxies — techniques: interferometric

1. INTRODUCTION

The 16 mag quasar 3C 345 (redshift $z = 0.595$) presents one of the best examples of apparent superluminal motion in a core-dominated extragalactic radio source. The source is a prominent and variable active galactic nucleus (AGN) in regimes from radio to UV (Bregman et al. 1986) but only a weak X-ray emitter (Ku, Helfand, & Lucy 1980). It exhibits properties typical of blazars (Impey & Neugebauer 1988) and of high-polarization quasars (Moore & Stockman 1984). The kiloparsec-scale radio structure of 3C 345 consists of a compact region at the base of a jet that extends over 3″ and terminates in a hot spot (Browne et al. 1982); there is a faint halo (Schilizzi & de Bruyn 1983). The jet is nearly straight over most of its length (Kollgaard, Wardle, & Roberts 1989).

The parsec-scale structure of 3C 345 has been studied for two decades at centimeter wavelengths with very long baseline interferometry (VLBI). Detailed imaging with global VLBI arrays and monitoring of structural changes have been pursued since 1979 (Unwin et al. 1983, hereafter U83; Biretta, Moore & Cohen 1986, hereafter BMC86). The VLBI images show typically a central unresolved emission region with flat radio spectrum (the "core"), and several partially resolved features that appear to be separating from the core with apparent speeds β_{app} ranging from $2c$ to $10c$; on parsec scales, the jet shows significant curvature. The core itself has remained stationary (Bartel et al. 1986; Tang et al. 1990). In high dynamic range images, faint filamentary emission underlying the moving features has been detected (Unwin & Wehrle 1992), strengthening the interpretation of the compact radio structure as that of a jet originating at the core and transporting material toward extended emission regions at kiloparsec distance from the central region. The superluminal features typically have steep radio spectra and show flux density variations. In one instance acceleration was observed (Moore, Readhead, & Bååth 1983).

This paper discusses VLBI observations at 22, 11, and 5 GHz made during 1984.76–1988.18. Observations are

TABLE 1

VLBI OBSERVATIONS AND IMAGE PARAMETERS

Epoch (yr)	ν_{obs}[a] (GHz)	Antennas[b]	Mk[c]	S_{cln}[d] (Jy)	θ_1[e] (mas)	θ_2[e] (mas)	ϕ[e]	DR[f]
1984.76.....	22.230	bs-gyo	II	9.21	0.388	0.186	−18°87	100
1985.75.....	22.230	bk-go	II	6.70	0.480	0.216	−16.86	100
1986.40.....	22.239	sb-rkgo	II	5.28	0.323	0.202	−5.02	130
1986.87.....	22.229	sb-lkyo	II	5.51	0.367	0.184	−16.09	100
1987.42.....	22.229	sb-lkyo	II	4.35	0.427	0.181	−13.53	50
1988.16.....	22.230	sb-lkgo	II	4.94	0.440	0.189	−18.12	100
1984.95.....	10.674	lb-kgfo	III	8.87	0.819	0.402	−12.86	150
1985.93.....	10.651	(l)-kg(f)ho	III	9.88	1.291	0.808	−3.34	300
1987.15.....	10.650	l-kgho	II	9.47	0.967	0.377	−6.65	200
1988.17.....	10.649	bl-kgfo	II	8.56	0.984	0.452	−17.66	50
1984.25.....	4.992	slb-gfyohe	II	7.48	1.363	0.830	−18.22	200
1985.77.....	4.992	sbw-jlkinyo	II	9.12	1.790	0.896	−17 46	200
1986.90.....	4.991	sbw-jgknyo	II	10.00	1.571	0.953	−18.20	500
1988.18.....	4.990	sbl-(n)kgyo	II	8.01	1.824	0.817	−15.30	500

[a] DC edge of recorded sky frequency band; bandwidth was 2 MHz for Mark II, and 28 MHz for Mark III.

[b] Participating VLBI observing stations and antenna diameter; the dashes separate observatories in the European VLBI Network and affiliates and those of the US VLBI Network; parentheses indicate that data from that station were not used for imaging analysis because of technical problems. b—Max-Planck-Institut für Radioastronomie, Effelsberg, FRG (100 m); f—G. Agassiz–Harvard Radio Astronomy Observatory, Ft. Davis, TX (25 m); g—National Radio Astronomy Observatory, Green Bank, WV (43 m); k—Haystack Observatory, Westford, MA (37 m); l—Istituto di Radioastronomia, Medicina, Italy (32 m); n—Naval Research Laboratory, Maryland Point, MD (26 m); o—Owens Valley Radio Observatory, Big Pine, CA (40 m); r—Crimean Astrophysical Observatory, Simeiz, Ukraine (former USSR; 22 m); s—Onsala Space Observatory, Onsala, Sweden (20 m); y—National Radio Astronomy Observatory VLA, Socorro, NM (25 m).

[c] Recording mode.

[d] Total CLEAN flux in the image.

[e] Major and minor axes of CLEAN beam, and position angle.

[f] Dynamic range of image.

described in § 2; images and a quantitative analysis based on model fitting to the visibility data are presented in § 3. Section 4 focuses on kinematic results, especially the apparent trajectories of the component motion. In § 5, we apply synchrotron self-Compton theory to derive a simple model that can account for the overall energy output from the source.

We adopt a parameterized Hubble constant and deceleration parameter of $H_0 = 100\,h$ km s^{-1} Mpc^{-1}, $q_0 = 0.5$. These give a luminosity distance to 3C 345 of $D_l = 1.99\,h^{-1}$ Gpc. An angular size or separation of 1 mas corresponds to $3.79\,h^{-1}$ pc. A proper motion of 1 mas yr^{-1} translates into a speed of $\beta_{app} = 19.7\,h^{-1}$. We use a definition of spectral index $S \propto \nu^{\alpha}$.

2. OBSERVATIONS AND DATA REDUCTION

3C 345 was observed at 5, 11, and 22 GHz in 14 sessions of the Global VLBI Network during the period 1984–1988 with the VLBI antenna arrays listed in Table 1. During 12 sessions, the Mark II VLBI recording system (Clark 1973) was used to record an effective bandwidth of 1.8 MHz. The Mark III system was used for two observations (Rogers et al. 1983). Typically, the stations were equipped with hydrogen maser frequency standards, allowing coherent integration of the correlated data with small amplitude losses. The data quality and calibration accuracy varied widely between observing sessions, owing to different weather conditions and changes in performance of the individual observing stations (e.g., antenna gain, local oscillator stability, antenna pointing accuracy, receiver noise and stability, and recording/playback quality). Finally, the sampling and coverage of the (u, v) Fourier transform plane by the visibility measurements varied between epochs, with the number of available antennas and the fraction of successful observing time.

The Mark II data were correlated with the JPL-Caltech Block 0 and Block II VLBI correlators, and then analyzed with the NRAO's AIPS software.[1] The data from all epochs were treated in a similar fashion: station-based interferometer delays and fringe rates were calibrated using the global fringe-fitting method (Schwab & Cotton 1983), with an initial point-source model (Walker 1989). No significant improvement in the detection of weak fringes was obtained in tests employing more different (more complex) starting models. (For the Mark III epochs 1984.99 and 1985.93, the solutions were derived independently for each baseline.) The fringe-fitted data were coherently averaged to 2 minutes, which limited amplitude losses to less than 2%, except for certain baselines at 22 GHz which were degraded by less than 5%. The visibility amplitudes from all epochs were calibrated using measured system and antenna temperatures, or telescope gain curves; measurements that were obviously corrupted by systematic effects were removed from the data sets.

The visibility data were analyzed for structural information with the Caltech VLBI software (Pearson 1991). Images were made using the "hybrid mapping" and self-calibration technique (Pearson & Readhead 1984). At a later stage, we reanalyzed all images in a consistent fashion using the Caltech implementation (DIFMAP) of the difference mapping technique (Shepherd, Pearson, & Taylor 1994).

[1] The National Radio Astronomy Observatory is operated by Associated Universities, Inc., under cooperative agreement with the National Science Foundation; AIPS is the NRAO's Astronomical Image Processing System.

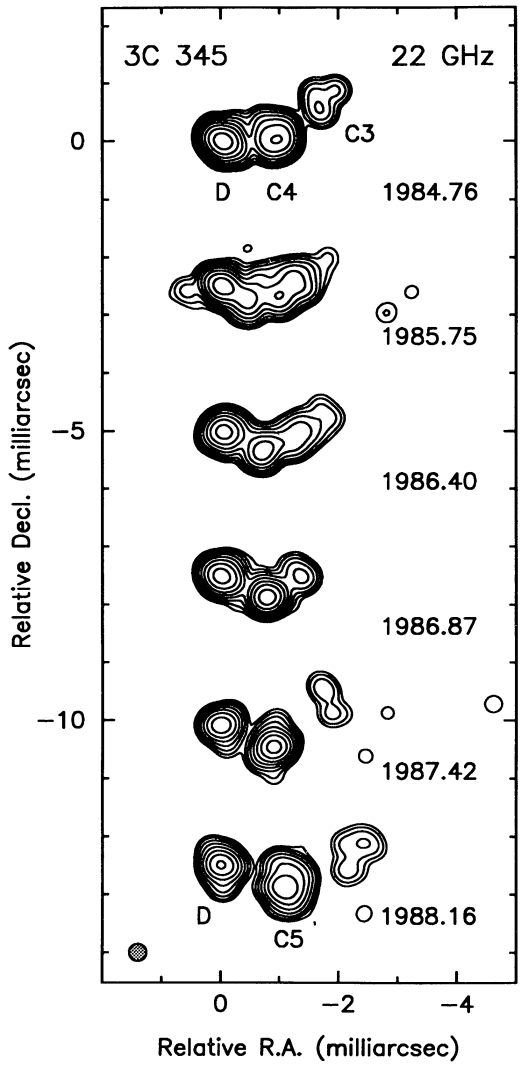

FIG. 1

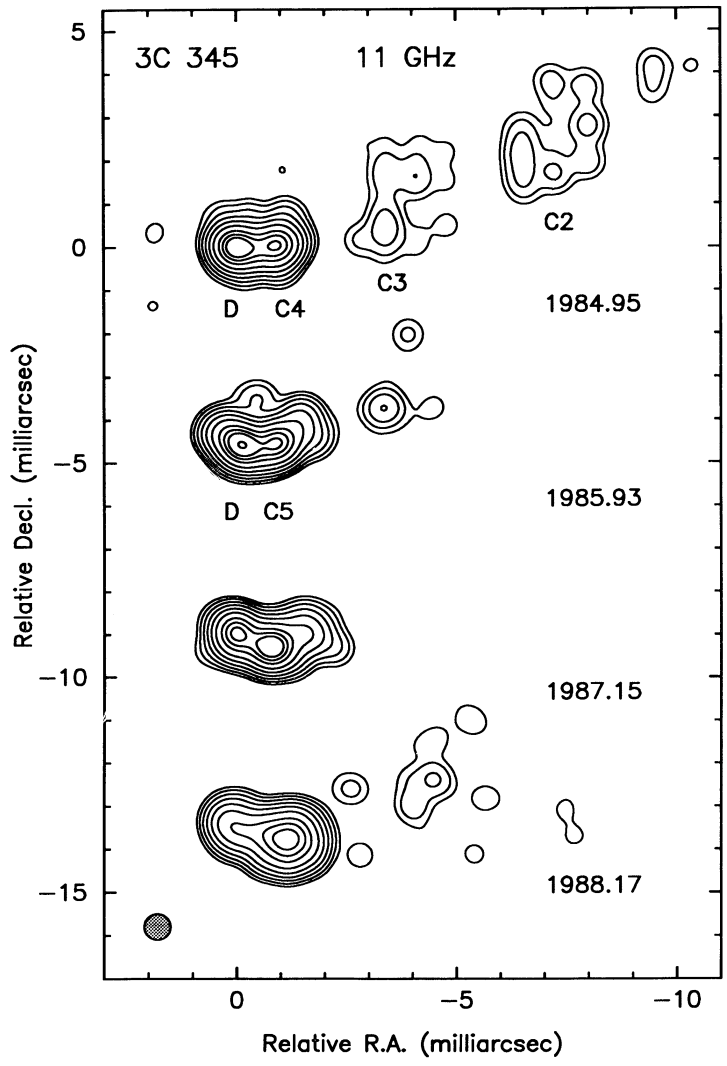

FIG. 2

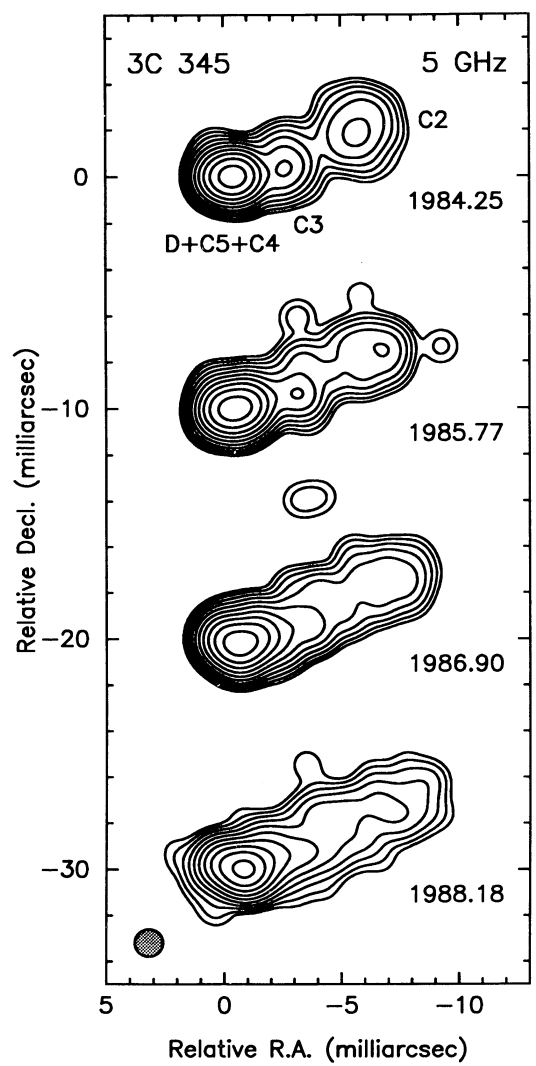

FIG. 3

FIG. 1.—22 GHz VLBI images of 3C 345. Contours are drawn at 10, 20, 40, 80, 160, 320, 640, 1280, and 2560 mJy/beam; there is no significant structure below −10 mJy/beam on any of these images. The CLEAN restoring beam is circular with FWHM 0.3 mas, shown as a shaded circle. Components are labeled following the convention of BMC86. The (arbitrary) coordinate origin is the position of the core "D" in the first image; the others are displaced equal steps in declination.

FIG. 2.—11 GHz VLBI images of 3C 345. Contours are drawn at 20, 40, 80, 160, 320, 640, 1280, 1920, 2560, and 3840 mJy beam^{-1}; there is no significant structure below −20 mJy beam^{-1} on any of these images. The CLEAN restoring beam is circular with FWHM 0.6 mas. Other details as in Fig. 1.

FIG. 3.—5 GHz VLBI images of 3C 345. Contours are drawn at 6, 12, 25, 50, 100, 200, 400, 800, 1600, and 3200 mJy beam^{-1}; there is no significant structure below −6 mJy beam^{-1} on any of these images. The CLEAN restoring beam is circular with FWHM 1.2 mas. Other details as in Fig. 1.

Figures 1–3 show the final images, combined by observing frequency. Several parameters are listed in Table 1: total CLEAN flux, size and orientation of CLEAN beam, and dynamic range (ratio of peak to lowest reliable brightness contour). We convolved the images at a given frequency with the same restoring beam, with a size approximately equal to a geometric average of the axes of the true beams.

For a quantitative analysis of the structure information in the images, we derived least-squares fits for models consisting of several optically thin, homogeneous spherical components to the visibility data of each observation (BMC86). These models are listed in Table 2; the parameters of the spheres are radius r from the reference (defined as the location of component D), position angle θ, and size ϕ. For the discussion below, we combined these fits with the observations during the period 1979–1984 (Biretta 1985; BMC86). The errors for models from this paper are formal 1 σ values, determined using the program ERRFIT in the Caltech VLBI software, which varies parameters of interest and examines the resultant $\Delta\chi^2$. Note that model parameters are often correlated, e.g., flux density and angular size of very extended components.

3. RESULTS

3.1. *Parsec-Scale Structure*

The VLBI images show the narrow and curved jet in 3C 345 on scales from $\sim$0.25 mas to $\sim$12 mas, corresponding to the region withing 1–45 h^{-1} pc from the nucleus (Fig. 1). The six images at 22 GHz have the highest resolution of this study, with $\sim$0.3 mas average beam size (corresponding to $\sim$1.1 h^{-1} pc). At this frequency, the source structure is typically (although not always) dominated by emission from the unresolved central region or core (labeled "D"). The core appears extended in the images when new structure features emerge which then develop into distinct components. We identify these components following the notation used by BMC86. The image from epoch 1984.76 shows D and component C4, and a westward extension that is probably associated with component C3 (BMC86). At later epochs, the structure is dominated by the new component C5 which first appeared as a core extension in 1985.75. C4 becomes increasingly resolved, although weak remnants are present in the 1988.16 image (which has somewhat superior dynamic range). At this last epoch in the sequence, bridging emission between D and C5 indicates another new component, C6.

The images made at 11 GHz have an average beam size of 0.6 mas (2.3 h^{-1} pc). The dynamic range in these images varies, owing to the data quality at different epochs. Therefore, features at large distances from the core are only marginally detected. C2 is reliably detected only in 1984.95. The dominating emission region in the east contains the core, and components C4 and C5. C5 appears separated from the core after 1985.93. By 1988.17, C4 is heavily resolved. Only remnants of the emission from components C2 and C3 are detected. In 1984.95, the core D (blended with component C5, which at that epoch was already seen at 22 GHz) and component C4 had approximately equal flux density. By 1988.17, C4 is faint and resolved, and D is significantly weaker than component C5, which then dominated the structure.

The 5 GHz observations (Fig. 3) probe the jet emission over the largest distance from the core in this work, covering a length of $\sim$12 mas (45 h^{-1} pc), at a resolution of $\sim$1.2 mas (4.6 h^{-1} pc). At this frequency, the jet appears to become smoother with time, and it is difficult to distinguish distinct components. We can identify three main regions; they correspond to the components C2, C3, and the blended complex D + C5 + C4. Qualitatively, the sequence in Figure 3 demonstrates the motion of C2 and C3, and their fading with time. At the later epochs, the eastern core region appears extended, reflecting the motion of C4 and C5 away from the core D.

The emerging "steady state" picture of the parsec-scale structure of 3C 345 is complemented by published VLBI observations. VLBI imaging at 43 GHz (Zensus et al. 1995) and at 86 GHz (Bååth et al. 1992) confirm the compact structure trajectories of C4 and C5 derived from Figure 1 and reveal further distinct features within the core region. Unwin & Wehrle (1992) obtained high dynamic range images at 5 GHz in 1989.28 and 1990.18, detecting emission from the jet (component C1) out to almost 70 h^{-1} pc. They confirm that the jet no longer merely contains a few well-defined emission regions. Instead, the structure is complex and of filamentary nature, suggesting more directly a collimated outflow. We are certain that this is a real effect, and not due to improvements in data and image quality with time. Rantakyrö et al. (1992) made images at 1.7 GHz in 1981.11 and 1985.27 which extend to 230 h^{-1} pc, and Matveyenko et al. (1992) made a VLBI image at 610 MHz which detects the jet over a scale of $\sim$450 h^{-1} pc. VLA observations (Kollgaard et al. 1989) show that the jet in 3C 345 is well defined on all scales out to 15 h^{-1} kpc before an apparent transition into an uncollimated structure occurs.

3.2. *Component Trajectories and Motion*

To analyze the apparent trajectory and motion for each component, we derived weighted least-squares fits to $x(t)$ and $y(t)$ (Table 2), the west and north position offsets (measured in milliarcseconds at epoch t) of the components referred to the core D (cf. Wardle et al. 1994). The results of the fits are tabulated in Table 3 and they are shown as dashed lines in Figure 4.

The fitting was performed using the data from this paper and BMC86 (cf. Biretta 1985). Program ERRFIT sometimes returned unrealistically small errors ($\ll$resolution), so to avoid undue emphasis of these points in curve fitting, we used errors σ that were enlarged in quadrature from the ERRFIT values (Table 2) by 15% of the average beam size (1.2 mas at 5 GHz, 0.6 mas at 10.7 GHz, and 0.3 mas at 22 GHz). We used weights σ^{-2}, and the following functional form of the fits:

$$f(t) = a_0 + a_1(t - 1985.0) + a_2(t - 1985.0)^2 + a_3(t - 1985.0)^3 + a_4(t - 1985.0)^4 . \quad (1)$$

The order of polynomials used for each component was chosen such that they reproduce the bends apparent in the trajectory. The inner components C4 and C5 required fourth-order fits (note the different number of nonzero coefficients for C5), whereas C3 and C4 could adequately be described with second-order fits. We also added ad hoc to each data set a point at the origin with infinitely small error, at an epoch T_0, chosen such that the expansion curves (see Fig. 5) extend through the point $(x(T_0), y(T_0)) = 0$. One could argue that the trajectories should *not* originate at the location of the core. However, this has negligible impact on the appearance of the curves over the range of actual measurements that are discussed here.

We did not fit the data for different frequencies separately, since the model fits do not indicate consistent offsets throughout. Such an effect is expected from physical models, although

TABLE 2

MODEL PARAMETERS

Epoch and Component	S (Jy)	δS (Jy)	r (mas)	δr (mas)	θ	$\delta\theta$	ϕ (mas)	$\delta\phi$ (mas)
1984.76 (22 Ghz; $S_{model}=9.0\pm0.4$ Jy):								
D	5.8	0.1	0.0	0.0	0°.0	0°.0	0.40	0.08
C4a	1.5	0.2	0.7	0.1	−89.1	1.4	0.39	0.08
C4b	1.3	0.3	1.0	0.3	−85.0	5.0	0.25	0.05
C3	0.3	0.1	1.8	0.1	−70.4	2.1	0.33	0.06
1985.75 (22 GHz; $S_{model}=6.4\pm0.2$ Jy):								
D	3.0	0.1	0.0	0.0	0.0	0.0	0.39	0.08
C5	1.8	0.1	0.5	0.1	−115.6	1.3	0.43	0.09
C4	1.6	0.1	1.0	0.0	−93.7	0.9	0.64	0.12
1986.40 (22 GHz; $S_{model}=5.0\pm0.4$ Jy):								
D	2.7	0.1	0.0	0.0	0.0	0.0	0.39	0.08
C5	1.6	0.1	0.7	0.1	−116.3	1.5	0.42	0.08
C4	0.5	0.3	1.2	0.1	−93.9	3.5	0.43	0.20
C3	0.2	0.1	1.8	0.4	−86.5	5.0	0.38	0.08
1986.87 (22 GHz; $S_{model}=5.6\pm0.1$ Jy):								
D	2.7	0.1	0.0	0.0	0.0	0.0	0.39	0.08
C5	2.5	0.1	0.9	0.1	−114.6	0.2	0.33	0.06
C4	0.4	0.1	1.3	0.1	−91.5	1.7	0.49	0.10
1987.42 (22 GHz; $S_{model}=4.1\pm0.1$ Jy):								
D	1.5	0.1	0.0	0.0	0.0	0.0	0.41	0.08
C5	2.6	0.3	1.0	0.1	−111.6	1.0	0.32	0.06
1988.16 (22 GHz; $S_{model}=5.1\pm0.1$ Jy):								
D	1.6	0.1	0.0	0.0	0.0	0.0	0.31	0.06
C5	3.0	0.1	1.2	0.1	−109.0	0.2	0.56	0.11
C4	0.5	0.1	2.2	0.1	−89.9	1.1	0.70	0.14
1984.95 (11 GHz; $S_{model}=8.3\pm0.3$ Jy):								
D	4.0	0.2	0.0	0.0	0.0	0.0	0.46	0.10
C5	1.2	0.2	0.5	0.1	−97.2	4.7	0.33	0.10
C4	3.0	0.2	1.0	0.1	−87.4	0.6	0.51	0.10
C3	0.1	0.1	3.6	0.2	−80.0	2.8	0.41	0.08
C2	0.1	0.1	7.5	1.5	−74.1	5.0	0.61	0.12
1985.93 (11 GHz; $S_{model}=9.9\pm0.7$ Jy):								
D	4.7	0.5	0.0	0.0	0.0	0.0	0.80	0.10
C5	3.0	0.5	0.7	0.0	−102.4	5.0	0.28	0.40
C4	1.7	0.2	1.3	0.1	−81.8	5.0	<0.40	0.08
C3a	0.28	0.1	3.1	0.6	−72.8	5.0	1.6	0.32
C3b	0.12	0.1	3.7	1.0	−78.4	5.0	1.8	0.36
1987.15 (11 GHz; $S_{model}=9.5\pm0.2$ Jy):								
D	3.6	0.1	0.0	0.0	0.0	0.0	0.59	0.12
C5	4.7	0.1	0.8	0.1	−110.0	2.0	0.63	0.12
C4	1.2	0.1	1.5	0.1	−88.3	2.0	0.83	0.16
1988.17 (11 GHz; $S_{model}=8.7\pm0.8$ Jy):								
D	2.3	0.6	0.0	0.0	0.0	0.0	0.78	0.16
C5	6.0	0.5	1.2	0.1	−113.7	4.4	0.77	0.15
C3	0.5	0.2	4.3	0.3	−80.0	3.5	0.66	0.13
1984.25 (5 GHz; $S_{model}=7.4\pm0.4$ Jy):								
D	2.6	0.3	0.0	0.0	0.0	0.0	0.57	0.12
C5	3.4	0.3	0.6	0.1	−85.9	2.0	0.39	0.08
C3	0.8	0.1	2.7	0.3	−81.4	2.0	1.69	0.34
C2	0.7	0.2	6.0	0.6	−70.2	5.0	2.51	0.50
1985.77 (5 GHz; $S_{model}=9.2\pm0.2$ Jy):								
D	2.6	0.1	0.0	0.0	0.0	0.0	0.00	0.00
C5	3.1	0.1	0.6	0.0	−93.7	1.6	<0.50	0.10
C4	1.7	0.2	1.2	0.0	−80.1	1.2	<0.50	0.10
C3	1.0	0.1	3.1	0.1	−79.0	1.2	2.10	0.10
C2	0.7	0.1	6.6	0.1	−68.8	3.0	2.9	0.30
1986.90 (5 GHz; $S_{model}=10.0\pm0.8$ Jy):								
D	1.5	0.2	0.0	0.0	0.0	0.0	0.27	0.06
C5	4.3	0.6	0.7	0.1	−112.0	3.0	0.70	0.30
C4	2.2	0.5	1.4	0.1	−87.3	1.3	1.03	0.30
C3	1.2	0.1	3.2	0.1	−78.8	1.5	3.47	0.60
C2	0.8	0.1	7.1	0.7	−69.9	5.0	4.02	0.80
1988.18 (5 GHz; $S_{model}=7.9\pm0.12$ Jy):								
D	1.3	0.1	0.0	0.0	0.0	0.0	0.68	0.10
C5	4.3	0.1	0.9	0.1	−103.0	1.3	0.96	0.19
C4a	0.8	0.1	2.0	0.4	−84.1	1.5	0.85	0.17
C4b	0.4	0.1	3.2	0.6	−82.0	5.0	1.39	0.28
C3	0.6	0.1	5.0	0.1	−77.0	1.1	3.52	0.70
C2	0.4	0.1	7.9	0.8	−69.1	3.0	3.55	0.70

NOTE.—Substructure is present in C3 at epoch 1985.93 (11 GHz) and C4 at epoch 1988.18 (22 GHz).

TABLE 3

POLYNOMIAL FITS TO COMPONENT TRAJECTORIES

Component	a_0	a_1	a_2	a_3	a_4	T_0	$T_{0.2}$
C2						1968.0	1969.40
$x(t)$	0.5917E+01	0.4284E+00	0.4724E−02	...	...		
$y(t)$	0.2109E+01	0.2222E+00	0.5772E−02	...	...		
C3						1976.0	1976.85
$x(t)$	0.2950E+01	0.2948E+00	0.1002E−01	0.1519E−02	...		
$y(t)$	0.4130E+00	0.1052E+00	0.96670E−02	0.3408E−03	...		
C4						1979.5	1981.45
$x(t)$	0.9727E+00	0.2235E+00	0.2055E−01	0.3171E−02	0.1787E−03		
$y(t)$	0.5132E−01	0.7044E−02	−0.2608E−01	0.1121E−02	0.1053E−02		
C5						1980.0	1984.35
$x(t)$	0.4238E+00	0.1473E+00	0.1546E−01	0.5840E−03	0.0E0		
$y(t)$	−0.1383E+00	−0.1108E+00	0.4188E−02	0.2648E−02	−0.3015E−03		

NOTES.—T_0 is the epoch of zero separation, included in the data for the fit (see text); $T_{0.2}$ is the epoch at which the core separation was 0.2 mas, derived from the fit. Note the different number of nonzero coefficients for C5.

the systematic errors in some of our model-fit positions are large and probably mask the effect of frequency dependence. BMC86 noted the frequency dependence of the measured separation between the core and the superluminal features, in particular C3 and C2 (see Fig. 5). During the period of the observations in this paper, both components were extended and the evidence for the above effect is marginal. This may be the result of measuring errors, but might also be caused by spectral index gradients. However, note that for both C4 and C5, the 22 GHz measurements lie systematically displaced from (below) the lower frequency points in Figure 5.

3.2.1. *Trajectories*

Figure 5 shows the trajectories $y(x)$ for components C2–C5. This analysis is based on the assumption that the core is stationary, in § 4.2.2 we will consider the possibility that the core

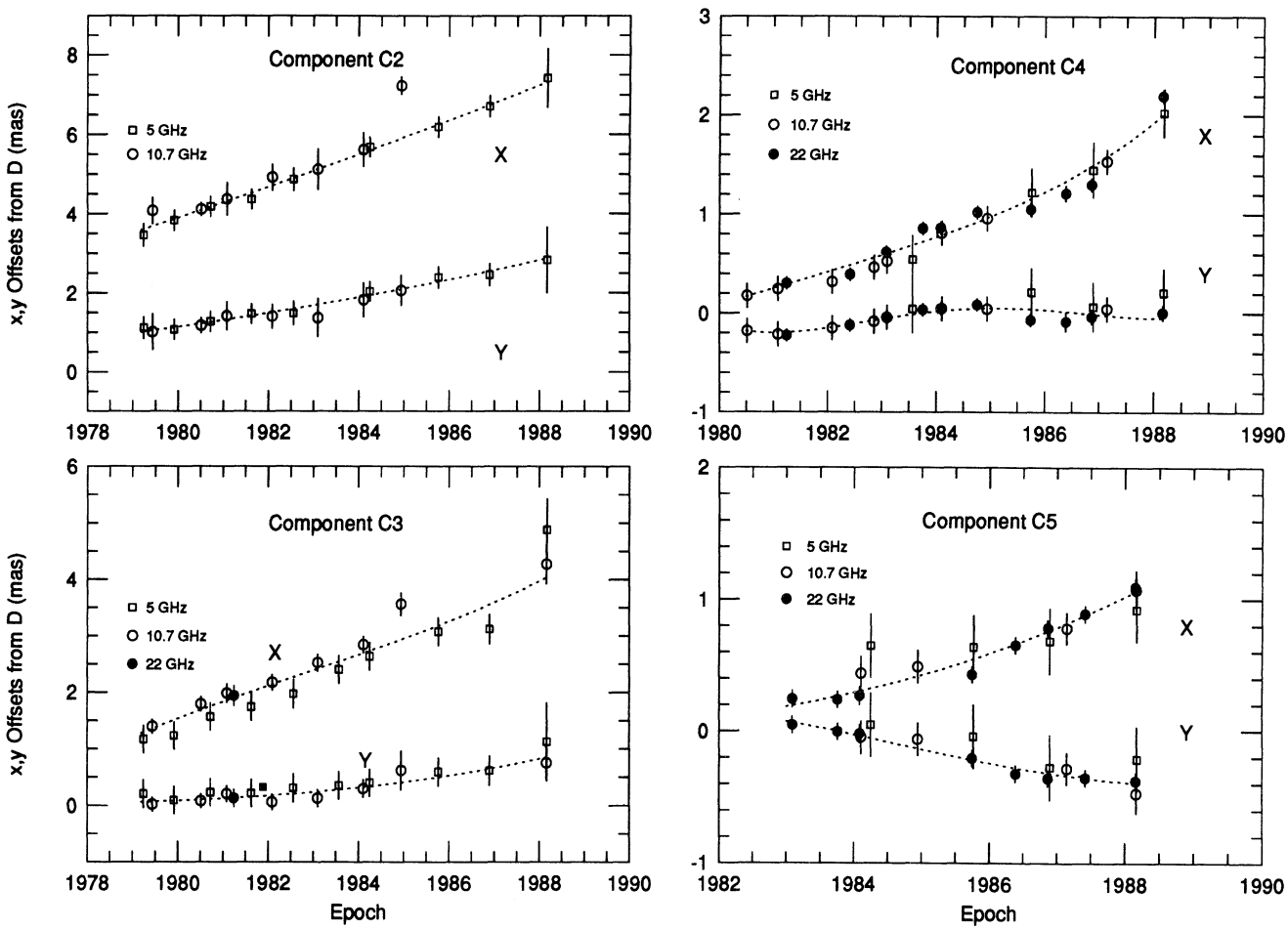

FIG. 4.—Polynomial fits of relative positions $x(t)$ and $y(t)$ for components C2–C5. Data are from BMC86 and this paper (see text).

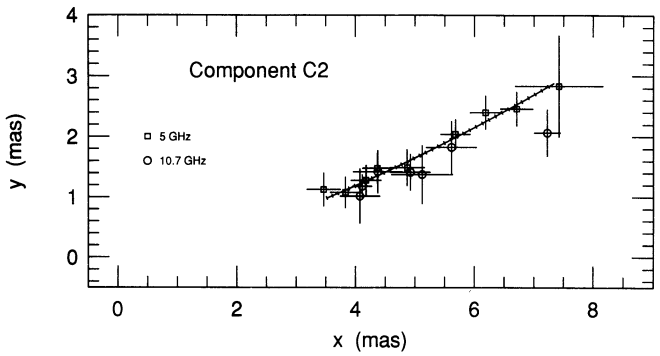

FIG. 5a

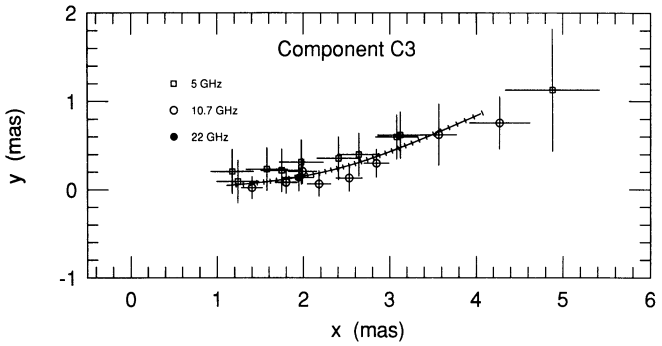

FIG. 5b

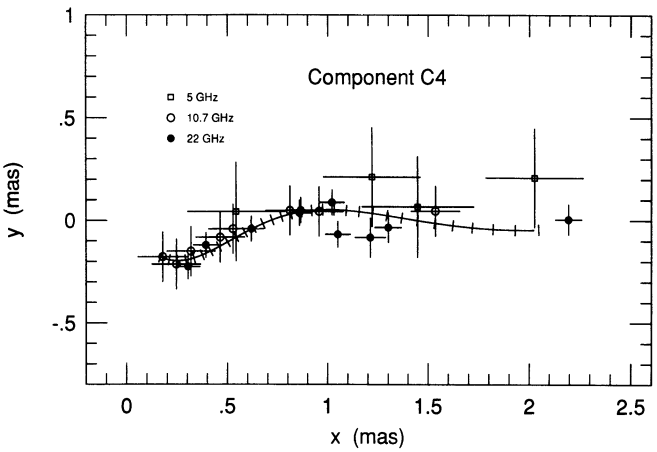

FIG. 5c

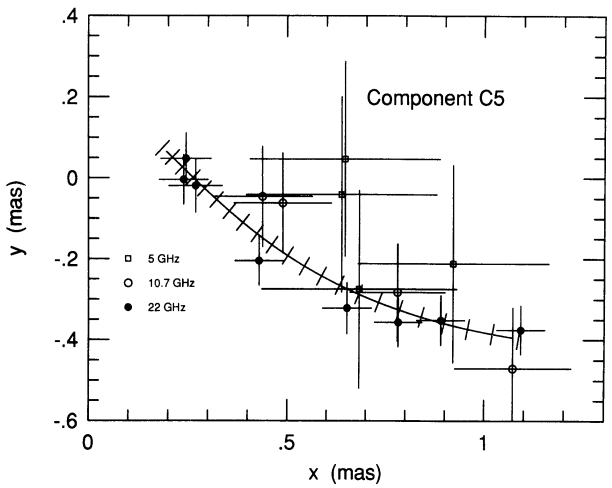

FIG. 5d

FIG. 5.—Trajectories of components C2–C5. Different symbols are used to distinguish observing frequencies. Drawn as solid lines are the fits $y(t)$ vs. $x(t)$ over the time range that was actually covered by our observations. Tick marks are equally spaced in time at an interval of 3 months and illustrate changes in speed along the trajectory. Note that the smooth trajectories represent fits to the time dimension (suppressed in these plots), as well as x and y.

is moving within the constraints of phase-referencing observations (Bartel et al. 1986).

Over the period covered by our and the previously published observations the apparent trajectories of all superluminal components in 3C 345 are substantially curved. This finding is in contrast to the notion that component trajectories are ballistic (Cohen et al. 1983). The latter was suggested based on straight-line fits through the origin that sufficed to describe observations covering shorter periods, except for component C4 which underwent a sharp kink at 0.4–0.5 mas from the core (BMC86; Moore et al. 1983). Note that the path of C2 could be described adequately by a straight line over the period it has been followed. However, although the positional uncertainty in the later observations is large, a straight-line fit would not extend to the location of the core, so by implication this component also followed a curved path.

Our observations also address the question whether subsequent components follow the *same* path as they separate from the core. At distances larger than 2 mas from the core, component C3 appears to follow approximately the same path as C2; i.e., it is not following a ballistic trajectory through the origin (Cohen et al. 1983).

Closer to the core, the situation is different. The curved trajectory for C5 does not follow that of C4. C5 appeared first in a position angle P.A. $\sim 280°$, whereas C4 had P.A. $\sim 225°$; however, in the later images C5 is curving toward the north, suggesting that it too will ultimately follow the path of C3 and C2.

VLBI observations at 43 and 89 GHz show new components closer to the core than those seen in our images. At 43 GHz, a new component (C6) has appeared at a position angle similar to that of C4 (Zensus et al. 1995), and even newer features have been seen in P.A. $-45°$ (Krichbaum and Witzel 1992; Bååth et al. 1992). Again, these seem to follow different apparent trajectories, although they still have to be tracked in detail, once they are clearly discernible at 22 GHz and below.

3.2.2. *Superluminal Motion*

From the model trajectories $x(t)$ and $y(t)$, we derived the instantaneous radial distance from the core $r(t) = [x(t)^2 + y(t)^2]^{1/2}$ and the instantaneous tangential proper motion $\mu(t) = (\dot{x}^2 + \dot{y}^2)^{1/2}$. Since the trajectories are curved, the tangential proper motion is an appropriate measure for the superluminal speed. For comparison, note that in BMC86 motions were derived from ballistic trajectories through the core or a chosen reference point.

In Figure 6*a*, we show $\mu(t)$ for C2–C5. Ranges of speeds and derived acceleration are given in Table 4. The apparent trend that the outer components have larger speeds than the inner ones becomes more significant if we consider μ as a function of

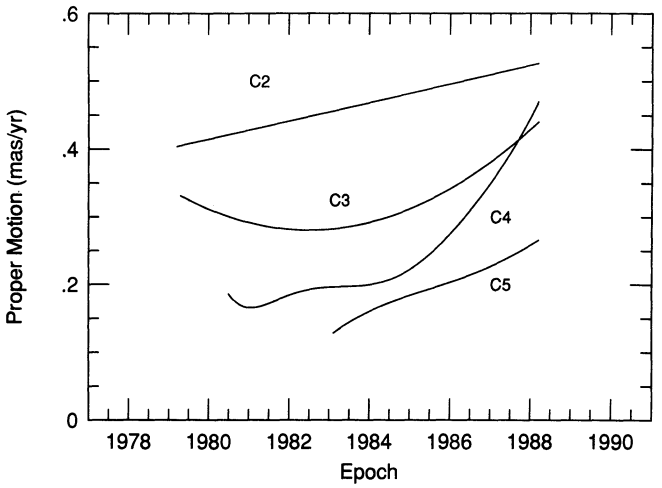

FIG. 6a

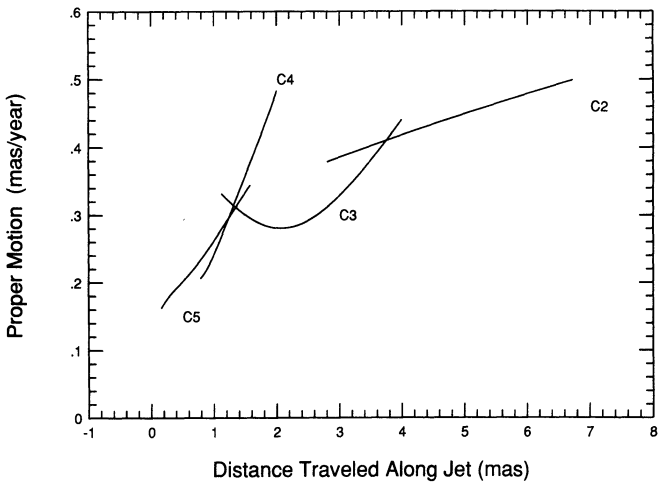

FIG. 6b

FIG. 6.—Speed of superluminal components in 3C 345. (*a*) Proper motion vs. time for components C2, C3, C4, and C5, measured along a tangent to the path of each component. (*b*) Proper motion vs. projected distance *s* along the curved component path on the sky from a point 0.2 mas from the core.

projected distance *s actually traveled* along the jet (Fig. 6*b*). A measure for this distance is given by the path integral along the trajectories in Figure 5. We chose as reference the point $T_{0.2}$ on the trajectory at separation 0.2 mas from the core (see Table 3), which can be determined for all components, despite the uncertainty due to extrapolation beyond the path segment over which observations are available. Figure 6 demonstrates an important conclusion: *component speeds increase with separation from the core.* We note the exception of C3, which around 1980 appears to slow down; this is probably an artifact, caused by the wavelength dependence of component positions, together with a slight bias of the fit for C3 to higher frequencies at early times (see Fig. 4).

Apparent superluminal motion is possible only for certain ranges of the kinematic parameters of the jet. From the measured apparent speeds β_{app}, we can derive limits for the Lorentz factor $\gamma = \beta \sin\theta/(1 - \beta\cos\theta)$ where βc is the component speed and θ is the component motion's angle to the line of sight (Pearson & Zensus 1987): $\gamma_{min} = (1 + \beta_{app}^2)^{1/2}$, and $\cot(\theta_{max}/2) = \beta_{app}$. Table 4 shows the allowed ranges for θ_{max} and γ_{min}. There is a progression from C2 through C5 toward larger θ_{max} and smaller γ_{min}, a reflection of the trend in Figure 6. However, since these are merely limits, one must be cautious about drawing conclusions from this trend. For instance, constant γ but varying θ with radius or time, or vice versa, are entirely consistent with the data (see § 4.2.1).

3.3. *Flux Density Evolution and Spectra*

The flux density changes of the VLBI components are shown in Figure 7. The total flux density of 3C 345 has been monitored by M. Aller and H. Aller since 1978 at 5, 8, and 15 GHz (Aller et al. 1985). At 22 and 37 GHz, the Metsähovi group obtained variability data during 1982–1990.5 (Teräsranta et al. 1992), and for comparison with the flux evolution of the components in our models, we display the total flux measurements in Figure 8 (M. Aller & H. Aller 1994, private communication; E. Valtaoja & H. Teräsranta 1994, private communication). The flux curves in Figure 7 are smooth and show only small variations in spectral index with time. They represent the sum of the evolution of several components simultaneously, unlike, for instance, OJ 287 for which there is an obvious correspondence between total flux and VLBI structure evolution (Hughes, Aller, & Aller 1989).

At the beginning of the period 1980–1988 covered by BMC86 and our observations, the total flux at centimeter wavelengths increased by ~50%, probably related to the appearance of component C4, which was first seen in 1980 (BMC86; Moore et al. 1983). That outburst began at high frequencies around 1979.0 and reached a maximum around 1981.5. In this phase, the total spectrum changed from flat to inverted ($\alpha > 0$), while the increase became apparent with delay and reduced amplitude at the lower frequencies. During 1982–1984, the overall spectrum once again flattened, and the flux level at all frequencies slowly decreased through 1988.

The flux density curves for D and C4 reflect the total flux behavior (Figs. 7*a* and 7*c*). Although the possible systematic uncertainties in the component fluxes are substantial, in the variations we can identify the same frequency behavior as for the total flux. C5 was first observed at 22 GHz in 1983, with only a small flux event visible in the monitoring data near

TABLE 4

SUPERLUMINAL SPEEDS IN 3C 345

Component	μ (BMC86) (mas yr^{-1})	μ (this paper) (mas yr^{-1})	$d\mu/dt$ (mas yr^{-2})	$\beta_{app} h$	γ_{min}[a]	θ_{max}
C2	~0.45	0.4 –0.53	+0.013 to +0.014	7.9–10.4	7.9–10.5	14°.5–10°.9
C3	0.3	0.28–0.44	−0.033 to +0.054	5.5–8.7	5.6–8.7	20.5–13.2
C4	0.3, 0.1	0.17–0.47	−0.063 to +0.117	3.4–9.3	3.5–9.3	33.2–12.3
C5	...	0.12–0.27	+0.019 to +0.037	2.4–5.3	2.6–5.4	45.9–21.3

[a] Limits γ_{min} and θ_{max} are derived from β_{app}, assuming $h = 1$; formulae including h are given in § 3.2.2.

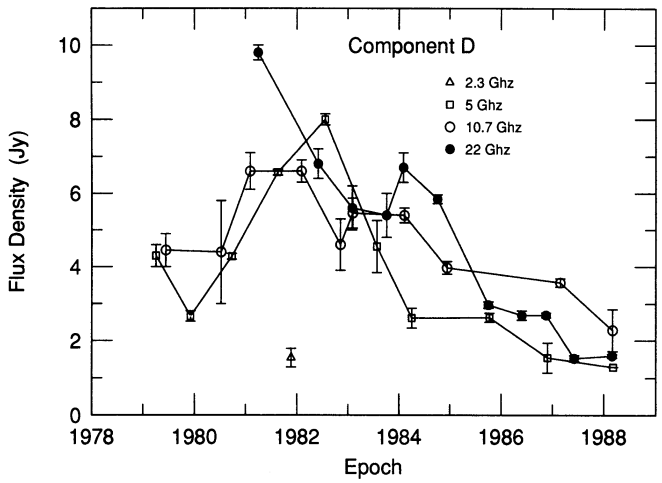

FIG. 7*a*

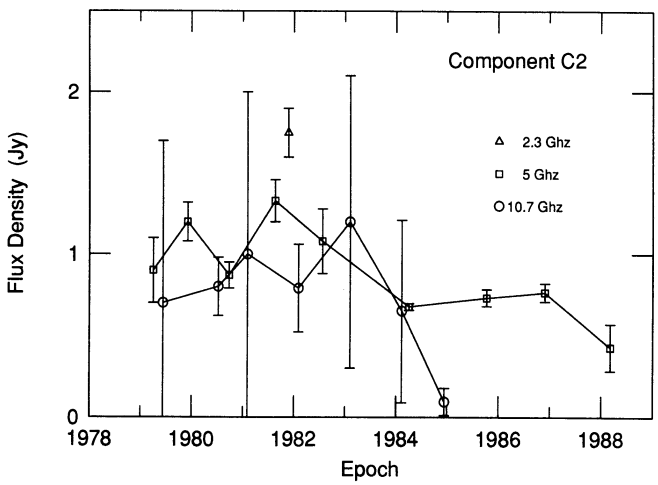

FIG. 7*b*

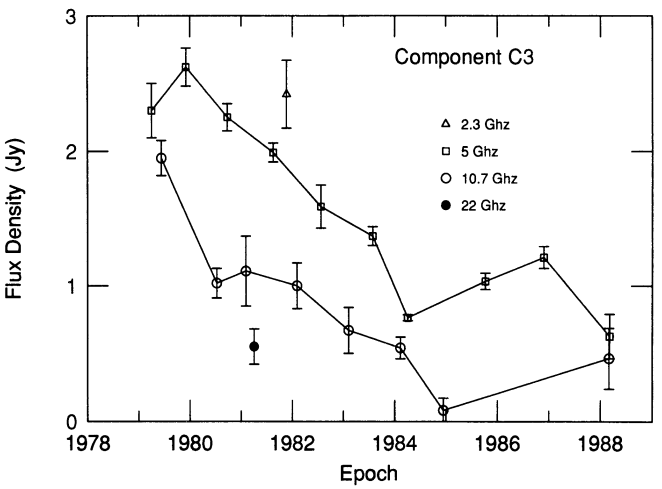

FIG. 7*c*

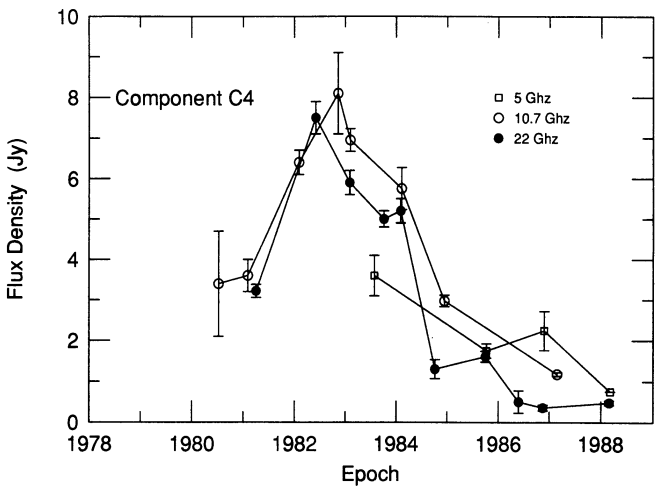

FIG. 7*d*

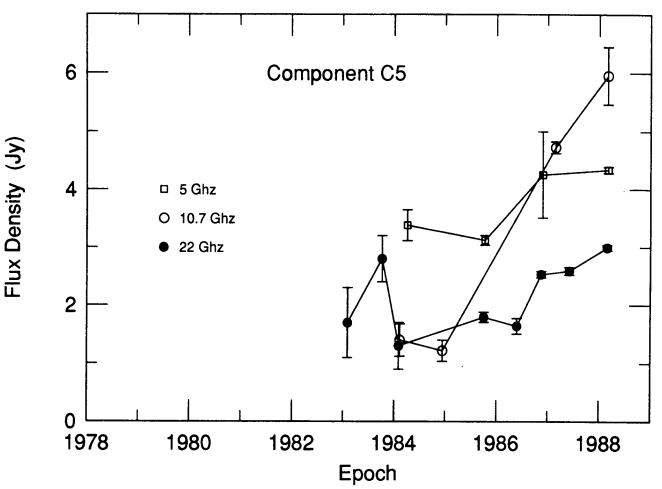

FIG. 7*e*

FIG. 7.—Flux density evolution of core D and components C2–C5. The data shown are from the models in Table 2 and BMC86. Solid lines connect successive points at a given frequency.

epoch 1982.25. Through 1988, it showed a steep spectrum, but this may be affected by the limited resolution. C3 slowly decayed with a steep spectrum through 1988, and the outer component C2 stayed at an unchanged flux level within the measurement errors. The dynamic range limitations of the higher frequency images prevent a clear identification of the spectral evolution for this component.

Flux curves of jet components as those in Figure 7 are useful in testing models for parsec-scale jets. Even though the time sampling of our VLBI observations is too sparse at any given frequency, our results can be used to constrain simple models. Rabaça & Zensus (1994) have shown that the flux density evolution of component C4 in Figure 7*c* can be reproduced in a parameterized shock model. They follow the approach of Valtaoja et al. (1992), which incorporates the central elements of "shock-in-jet" models (Marscher & Gear 1985; Marscher 1990) to explain total flux outbursts in compact radio sources. The results indicate that a shock associated with C4 would be strong with a magnetic field oriented largely parallel to the shock.

Lobanov & Zensus (1994) analyzed the spectral evolution of the jet features in 3C 345. They find a correlation between

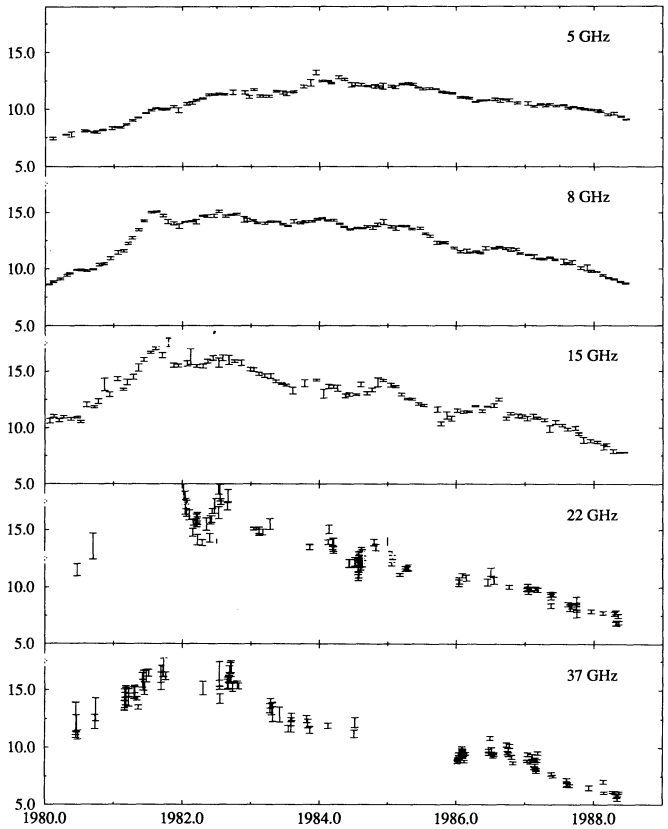

FIG. 8.—Total flux density measurements of 3C 345 at 5, 8, and 15 (M. Aller & H. Aller 1994, private communication) and 22 and 37 GHz (E. Valtaoja & H. Teräsranta 1994, private communication).

integrated flux and peak frequency in the component spectra, and also differences between the changes in the spectrum of the core and the superluminal features. These might be reconciled within the "two-fluid" model of Pelletier & Roland (1989).

4. KINEMATIC MODELS OF THE JET

Our results give a detailed account of the overall appearance and time evolution of the parsec-scale jet in 3C 345. The superluminal "components" observed for more than two decades are regions of enhanced emission traveling within the confines of an underlying continuous jet. The jet undergoes substantial wiggling near the core and is gently curved in the outer regions that reach into the kiloparsec-scale structure. The analysis in § 3 describes the kinematics (as observed on the plane of the sky), but it does not depend on the true nature of the components themselves: they might be isolated emission regions, or merely relatively minor perturbations or shocks within the jet which appear prominent because of Doppler-boosting effects. We now discuss what may be deduced about the large-scale jet orientation, then extend the analysis to modeling the three-dimensional structure of the jet.

4.1. *Large-Scale Jet Orientation*

The VLBI images trace the jet only to a projected distance $\rho \simeq 12$ mas from the core, but we can make some deductions about the jet orientation on much larger scales. VLBI observations with better short-baseline data and observations at lower frequencies show the jet out to component C0 at $\rho \simeq 60$ mas (Unwin & Wehrle 1992; Rantakyrö et al. 1992). VLA images with 300 mas resolution show the jet continuing to 3".8 (Kollgaard et al. 1989), and there is little doubt that the jet is continuous over this wide range of scales. The amorphous halo surrounding the arcsecond-scale jet suggests extreme projection effects on the large scale (Murphy et al. 1993). Jet curvature (defined as rotation of the ridge line per logarithmic radius interval) decreases monotonically with radius. The observations show strong curvature within $\rho < 0.5$ mas, but essentially no curvature beyond 4 mas (rotation within 8 mas is $\sim 70°$). Between 8 mas and the closest VLA knot at 900 mas, the ridge line rotates through a further 20°, but is essentially straight beyond that.

The large-scale orientation can be estimated by combining our proper-motion measurements with the above curvature data. The largest allowed (in this context, most conservative) θ furthest from the core is $\theta_{\max} = 11°$ for C2 (Table 4). If we assume that the 20° bend seen on the plane of the sky has a comparable perpendicular component $\Delta\theta$ (away from the line of sight), then $\Delta\theta \sim 20° \sin 11° = 3°.8$. Thus we estimate that the straight portion of the arcsecond-scale jet lies at $\theta_{\max} + 3°.8 \sim 15°$, corresponding to deprojection by a factor between 4 and 8, and a total jet length of $\sim 55\ h^{-1}$ kpc. If $\theta < \theta_{\max}$, then this size estimate is correspondingly increased.

4.2. *Three-dimensional Jet Models*

Superluminal motion requires that the jet must be relativistic and viewed at a small angle to the line of sight, which implies that projection effects are likely to be significant. Theoretical models have been advanced using VLBI observations to deduce the three-dimensional jet structure in 3C 345 and similar sources. Hardee (1987) applied a helically twisting model to 3C 345 data from 1981–1983, obtaining good agreement to this limited data set. Steffen et al. (1995) developed a helical jet model based on a larger body of data including this paper (cf. Camenzind 1986). Qian et al. (1991, 1992) discuss a model that reconciles the differences in trajectories by motion of the superluminal features along spiral-shaped magnetic field lines within the jet. For these theoretical approaches, the trajectories in § 3.2.1 represent the best currently available body of data.

In this section we consider kinematic models which enable us to infer the three-dimensional structure of the jet directly from our data and discuss three (of many) possible explanations for the strong curvature and increase in apparent speed of component C4: (1) Curvature of the jet in all three dimensions. In this scenario, γ varies modestly, if at all, and changes in θ account for the acceleration. (2) Real acceleration, i.e., increasing Lorentz factor γ with radius (or time), in which case the actual jet curvature is modest and θ (the angle of the instantaneous velocity vector to the line of sight) changes only slowly with radius. (3) Our choice of the core as a reference point for aligning the component positions is incorrect, and the apparent acceleration can be reduced in a suitably chosen reference frame.

Cases 1 and 2 represent two extrema within the range of ($\gamma(t)$, $\theta(t)$) combinations which yield the observed $\beta_{\rm app}$. There is a slight theoretical bias toward case 1, though the observations allow either, and both involve acceleration of the three-dimensional jet. The consequences of the two models for the jet dynamics are profound. Note that $\theta = \text{const}$ does *not* in general imply that the resulting path lies on the surface of a cone. Only certain curves, such as those discussed by Conway & Murphy (1993) satisfy this criterion. In general, both cases

yield complicated three-dimensional shapes, but as we will show below, case 1 is the most plausible, and we consider this case in detail and highlight the other possibilities.

4.2.1. *Projections of a Jet onto the Sky Plane*

The three-dimensional jet structure can be deduced from the curves $x(t)$ and $y(t)$, for either of case 1 or 2, provided that Doppler boosting or dimming [flux $\propto \delta^{3-\alpha}$, where the Doppler factor $\delta = \gamma^{-1}(1 - \beta \cos \theta)^{-1}$] is not too extreme, so that the curves reliably trace the actual jet path. Light travel time effects are ignored, so the projected paths correspond to a steady state.

If we assume γ = const as the jet curves (case 1), then we can solve for $\theta(t)$ using $x(t)$ and $y(t)$, provided $\gamma^2 - 1 > \beta_{\rm app}^2$ at all points along the trajectory. Two solutions $\theta(t)$ always exist for any γ satisfying the above inequality, and we designate these the "small-angle" and "large-angle" solutions. There is no a priori preference for either one. Once we have $\theta(t)$, the complete three-dimensional path can be derived by using $x(t)$ and $y(t)$ to solve for the third dimension, i.e., the component $z(t)$ of the jet along the line of sight. Since $\beta_{\rm app} > 1$ for all the parsec-scale components in 3C 345, the z-coordinate is large. Thus the paths, when viewed as $z(x)$ or $z(y)$, appear very straight for almost any allowed γ, which means that, if the jet were detectable at large angles to the line of sight, it would appear very long and almost perfectly straight.

We illustrate the results for component C4, which shows the most curvature of the four we have studied. To permit solutions at all radii of interest, we selected $\gamma = 11$, slightly larger than required by the largest $\beta_{\rm app}$ along the curve in Figure 5*c*, and selected the small-angle solution. For C4, $\theta \approx 1°$ at ≈ 0.2 mas and increases monotonically with radius to $\sim 4°$ at ≈ 2 mas. The solution is plausible, because it explains (a) the increase in superluminal motion with radius—θ is smaller than the critical angle γ^{-1} but increases toward it; (b) that the jet bending is strongest near the nucleus—a smooth intrinsic bend would be more amplified nearer the nucleus; (c) that the flux density of C4 varies only by a factor ≤ 10 (Fig. 7), and some of this evolution may be due to a modest decline in the Doppler boost factor $\delta^{3-\alpha}$ by a factor of ~ 3. By contrast, the large-angle solution, for which θ ranges between 32° and 9°, perhaps is a priori more probable because the available solid angle is larger, but is less appealing. While equally valid as an explanation for (a), it does not naturally lead to (b), and (c) poses a serious problem because $\delta^{3-\alpha}$ *increases* by a factor of ~ 3000 along the path of C4. We do not know how rapidly the luminosity of a jet component evolves, but a fortuitous balance between Doppler boosting and intrinsic evolution seems contrived.

Applying the same analysis to the other superluminal components we draw very similar qualitative conclusions, since apparent acceleration is seen in them also (Fig. 6). From a similar analysis, Roberts & Wardle (1994) also favored the small-angle solution for components C2 and C3.

In three dimensions, the path of C4 is very straight for most viewing angles, as shown above. A more interesting question is to ask how the jet would appear when viewed by an observer whose line of sight to the source differs only slightly from our own. In this way we can determine whether the projection we observe on the sky is "special" in some way. In the center panel of Figure 9 we show the curve $y(x)$ representing the observed path of C4 for the small-angle solution. The surrounding panels show the appearance on the plane of the sky for lines of sight which lie at an angle $\omega = 2°$ to our own; we show eight different position angles (η) of these lines of sight, at intervals of 45° rotation about our line of sight.

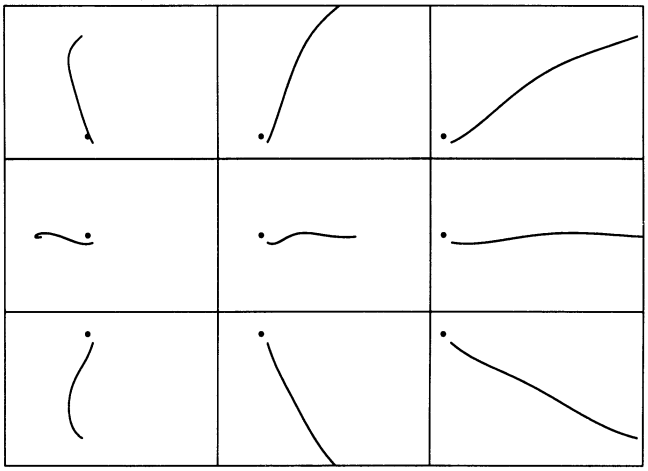

FIG. 9.—Projections of the three-dimensional path of component C4 onto the plane of the sky. The size of each panel is 4.9 × 3.5 mas. The center panel shows the path fitted to the observational data (same as Fig. 5), with the nucleus represented as a dot. Surrounding panels show the result of rotating the jet by an angle $\omega = 2°$ about an axis in P.A. η in the plane of the sky. Clockwise from the top left panel, values of η are 45°, 90°, 135°, 180°, 225°, 270°, 315°, and 0°. These projections assume (in a simplification) that $\gamma = 11$, i.e., independent of time, and that the jet emission is steady state, allowing us to ignore light-travel time effects.

There are several points to notice: (1) For any moderately straight jet, there will always be a combination of these parameters which results in extreme foreshortening and distortion. In this case, the middle-left panel shows the jet highly foreshortened and distorted since for that case $\theta \sim \omega$ over most of its length. (2) Except for this orientation, the jet appearance is not a strong function of ω or η, and most orientations show modest curvature. As expected, the most obvious change is the overall projected length of the jet. (3) Sharp curvature persists in many orientations within 0.5 mas of the core. In that radius range $\beta_{\rm app}$ is small, hence $\theta \sim \omega$, which makes the appearance less sensitive to the viewing direction. (4) Effects of Doppler boosting are ignored [though they could be readily computed from $x(t)$ and $y(t)$]. For example, the jet represented in the middle right panel of Figure 9 would appear ~ 5 times fainter than an identical jet as represented in the center panel.

Case 2 takes the other extreme assumption, namely, θ = const, and it also yields a curved jet. A single solution exists for γ for all $\beta_{\rm app} < \cot(\theta/2)$, though for $\beta_{\rm app} \simeq \cot(\theta/2)$ the resulting γ may become implausibly large. We generated projection plots analogous to Figure 9, trying several combinations of θ and ω. Perhaps surprisingly, the results were qualitatively similar. For example, assuming $\theta = 2°$ and $\omega = 2.°5$ results in curves which are somewhat straighter, but otherwise very similar to those in Figure 9. As noted above, a constant-θ jet is rather contrived, since our viewing direction has to be special at all points along its length.

We conclude that the curvature and acceleration can be naturally explained as projections of a three-dimensional jet for which $\gamma \simeq$ const, but we cannot rule out the θ = const case. Unfortunately it is not straightforward to separate intrinsic variations from changes due to this geometric factor; otherwise, we could have used the component flux density evolution (§ 3.3) to constrain the allowed geometry via the Doppler-boost factor. Note that a substantial fraction (perhaps as much

as 50%) of the decay in flux density of the individual components can be expected from changes in Doppler-boosting factor as the trajectory bends away from the line of sight.

Polarization data, interpreted in the framework of a specific shock model, can provide additional strong constraints on jet geometry. Wardle et al. (1994) discuss how VLBI polarization imaging data can be used in this way. Eventually, a combination of these methods should yield powerful enough constraints to discriminate between detailed physical mechanisms operating in relativistic jets.

4.2.2. *Proper Motion of the Core*

Here, we consider case 3, relaxing the fundamental assumption that the quasar core "D" is a reliable reference point [the origin $x(t) = 0$ and $y(t) = 0$] to align the various images (Fig. 10*a*). Obviously, if the nucleus is not fixed, but has a proper motion of its own, then the trajectories will shift in the sky. This possibility was motivated by the fact that C5 moves more slowly and in a very different direction from other components. We consider only the simplest case of rectilinear motion, but a more complicated trajectory might arise if the jet emanates from one of a pair of closely orbiting black holes (Begelman, Blandford, & Rees 1984; Camenzind 1993). We selected a velocity vector of the core in the plane of the sky which makes the tracks most nearly parallel (Fig. 10*b*). For this choice, the core is moving at 0.2 mas yr^{-1}, in P.A. $-60°$, crossing the origin at epoch 1981.1; all tracks form a narrow band in P.A. $\simeq -65°$. This model is of course purely kinematic: the core velocity itself is superluminal ($\beta_{core} = 3.9$), but it illustrates how critical the above assumption is to the interpretation of the kinematics.

Note that the trajectory of C2 is hardly affected (though stretched out), while C4, and especially C5, look very different. The measured proper motion of C5 is much slower than the others and in a very different position angle—vector addition of the core velocity results in trajectories which now lie closer to parallel. This implies a simplification of the kinematics: viewed from the reference frame of the moving core, new components are ejected in a *single* favored direction, but at differing speeds. A prediction of this model is that new components will parallel C2's track if fast, and C5's track if slow.

If the correct reference frame for the core is defined by the grid of quasars, then the measurement of the core proper motion relative to NRAO 512 (Bartel et al. 1986) rules out this model, though not at high significance. Their data are from 1971–1982 (weighted strongly toward 1980–1982, whereas our model applies to data from 1984–1988), so it is possible that the speed has changed or that the reference point is now physically different. A single new measurement should settle the question. Such a high speed is physically very implausible if the VLBI core is stationary relative to the (presumably massive) central energy source, even if in a tight binary orbit, but not if the component we identify as the core is itself a feature in a relativistic jet.

5. SYNCHROTRON SELF-COMPTON MODEL

Apparent superluminal motion and other properties observed in 3C 345 and similar core-dominated radio sources have been explained as resulting from bulk relativistic motion in two oppositely directed jets of plasma originating in the nucleus of the source (Blandford & Königl 1979; Blandford 1987). Thus the optically thick core in VLBI maps represents the base of the jet (located near the apex of the jet cone), and the superluminal components are regions of enhanced emission moving along the jet. While these general properties of this "standard model" are well established (Pearson & Zensus 1987), in-depth comparisons between observations and detailed models have generally been unsatisfactory. This is in part caused by the fact that VLBI images often lack sufficient detail or time coverage and that physical models typically possess many free parameters and lead to ambiguous results.

In this section we present a physical model for 3C 345 that is constrained by VLBI and multiband flux density observations and yields an estimate of the overall density profile and energetics of the source. X-ray observations provide an important constraint, because inverse Compton emission from the VLBI-scale radio components may contribute significantly to the observed flux and because they force the conclusion that the emitting material is moving relativistically.

This model is a specific version of the standard model defined above, and it idealizes the source as consisting of several distinct regions moving out relativistically and emitting in the radio (synchrotron) and X-ray (synchrotron self-Compton). Theory predicts the X-ray flux from these regions (Jones, O'Dell, & Stein 1974; Blandford & Königl 1979), and an excess of predicted over observed X-rays is interpreted as evidence for bulk relativistic motion (Cohen 1985; Marscher

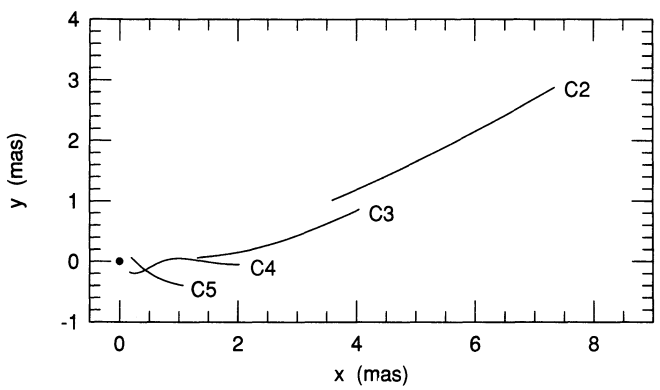

FIG. 10*a*

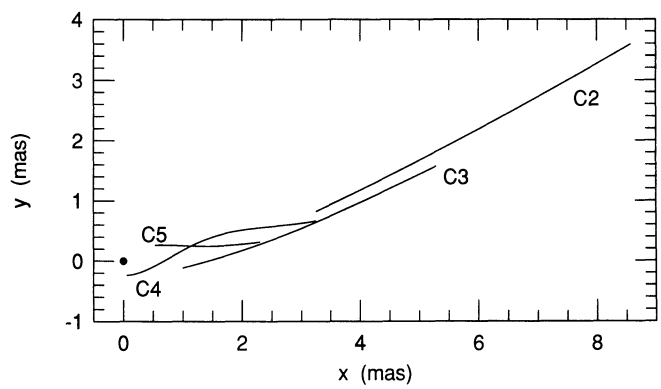

FIG. 10*b*

FIG. 10.—Trajectories of components C2–C5, on the plane of the sky. (*a*) All apparent trajectories from Fig. 5 combined. (*b*) The effect of replacing the quasar core with a reference point moving at 0.2 mas yr^{-1}, in P.A. $-60°$, and crossing the origin at epoch 1981.10.

1987). This may be used to constrain or restrict ranges of model parameters. The virtue of this approach over more complicated but perhaps more realistic calculations (Ghisellini, Maraschi, & Treves 1985; Band & Grindley 1986; Maraschi, Ghisellini, & Celotti 1992) is the fact that it has a relatively small number of free parameters.

To restrict the parameter space, we make additional simplifying assumptions: (1) the fluid speed is not a function of radius or time; (2) the VLBI "core" D is a partially opaque $\tau \sim 1$ region of emission near the apex of the conical jet; (3) the superluminal components C2–C5 dominate the radio emission outside the core; and (4) these components can be represented as homogeneous spheres. For this discussion we ignore the kiloparsec-scale low-frequency radio emission. It is generally believed that the large-scale radio emission requires a continuous energy supply, but we do not attempt to use this as a constraint. We use Königl's (1981) theory of a smooth inhomogeneous jet with conical geometry to model the core. A key feature of this model is that it explains an ubiquitous property of powerful compact radio sources, including 3C 345—a flat spectrum for the observed radio core. Another feature is that the core appears located closer to the apex of the cone with increasing frequency; this has been used to explain the frequency dependence of the distance between the core D and component C3 (BMC86).

We constrain the predicted inverse Compton X-ray flux not to exceed the observed value and derive a lower limit on the Doppler factor δ for the spheres (Cohen 1985; Marscher 1987) and for the jet. The final step is to combine the sphere and jet models to determine a consistent parameter set that describes the overall energetic properties of the source. This "combined model" has two features which differ from previous approaches: (1) the Doppler factor is *not* independent of h, as it is for a sphere, because the jet is aspect sensitive; and (2) the constraints from proper motion and the observed X-rays combined give well-defined limits to γ and θ which are fairly insensitive to the chosen model parameters. Unwin et al. (1994) applied this method, though they did not explore dependence on h.

The calculations require knowledge of the total X-ray flux density, the overall spectrum, the radio spectrum and size of each spherical component, and, for the jet component, the jet opening angle, the integrated spectral index, and the peak flux density. Typically, at any given epoch, the spectrum and size are not equally well determined for all components, mainly because the source may not be monitored frequently enough. BMC86 analyzed the spectrum for epoch 1982.0, and we also selected this epoch, for which sufficient information is available to derive a combined model accounting for the emission from all components. Note that Unwin et al. (1994) show that during 1992 the X-rays from 3C 345 were dominated by component C5; earlier work (U83) identified C3 as the main source of inverse Compton X-rays during 1979. We show below that C4 and the core were the regions dominating the X-rays near epoch 1982.0.

For the X-ray flux density we used the *Einstein* satellite measurement $S_{\rm Xobs} = 0.7$ μJy at 1.0 keV (Ku et al. 1980; Worrall & Wilkes 1990) made at epoch 1979.8; the fitted spectral slope over the observed 0.5–4.5 keV band was $\alpha = -0.43$. Another measurement was made at epoch 1989.32 with the *Ginga* satellite in the overlapping 2–10 keV band, giving $S_{\rm Xobs} = 0.57$ μJy at 1.0 keV, and $\alpha = -0.4$ (Makino 1989), indicating no strong variability. Later *ROSAT* observations indicate that the source may be slightly variable below 1 keV (Unwin et al. 1994). In this analysis, we assume the X-ray spectrum is a nonvarying power law, but this is not critical because the value of $\delta_{\rm min}$ we derive is proportional to only a small power (~ 0.2) of $S_{\rm Xobs}$. A comprehensive broadband radio–X-ray spectrum of 3C 345 was compiled for the period 1983 April–May by Bregman et al. (1986).

5.1. *The Spherical Components*

We model the superluminal components in 3C 345 as homogeneous spheres of angular diameter ξ, containing a tangled magnetic field B and relativistic electrons which give a synchrotron spectrum with optically thin index α and maximum flux density S_m at frequency ν_m. Each sphere radiates inverse Compton X-rays, giving a flux density $S_{\rm X,IC}$. The calculation for $S_{\rm X,IC}$ implicitly assumes Doppler boosting of the form $S \propto \delta^{3-\alpha}$, which is correct for optically thin spheres. Since the inverse Compton flux cannot exceed the observed X-ray flux (but other X-ray emission mechanisms could be operating simultaneously), the calculation yields a lower limit to δ (Marscher 1977); this limit may be applied separately to each component.

We assume that the moving components are spheres in order to simplify the calculations. (Note that calculations for a slab geometry, perhaps preferable in case of a thin shock, yield similar results.) In reality the components will not be homogeneous and may contain filamentary structure. For example, C2 is clearly nonspherical in recent detailed images (Unwin & Wehrle 1992). To partially compensate for this we introduce a filling factor f, whose effect we approximate by reducing the diameter of a sphere by $f^{1/3}$. In this section we use $f = 1$ because our main result is a lower limit to the Doppler factor and $f = 1$ is the most conservative assumption. In the next section we discuss the energetics and show that $f = 0.3$.

The spectral information for an individual component is limited by the frequency coverage and quality of VLBI measurements near a given epoch, and rarely are α, ν_m, and S_m well defined. Therefore, we chose self-consistent values that matched the data and gave a reasonable fit to the overall spectrum when all components and the core are considered together (Fig. 11).

Observational data and results from the X-ray calculation are given in Table 5. Columns (2)–(7) summarize the observational data, taken from BMC86 and this paper. For C2 and C3 we use the highest value for ν_m which is consistent with the data. For C4 both the spectral peak and index are unknown and we use a representative possibility. Column (5) gives the measured angular distances ρ between the centers of the components and the centroid of component D, measured at 11 GHz. Column (6) gives the measured angular diameters ξ and their errors, and column (7) gives $\beta_{\rm app} h$ for epoch 1982.0 from the proper motion curves in Figure 6.

The X-ray calculation yields the product $S_{\rm X,IC}\,\delta^{4-2\alpha}$ (col. [8]), derived from columns (1)–(6) using the formula from Marscher (1983), which is given in simple form for a sphere by Cohen (1985). The factor $\delta^{4-2\alpha}$ arises from the transformation of the observed radio turnover frequency and flux density from our rest frame to that of the emitting component. Column (9) is the lower limit to δ computed by setting $S_{\rm Xobs} = S_{\rm X,IC}$.

Parameters for C3 are reasonably well determined, and $\delta_{\rm min} = 3.6$ is a firm lower limit (Table 5). By itself this only demonstrates mildly relativistic motion. U83 give $\delta_{\rm min} = 8.1$ for C3 at the epoch 1979.7. The main reason for the discrep-

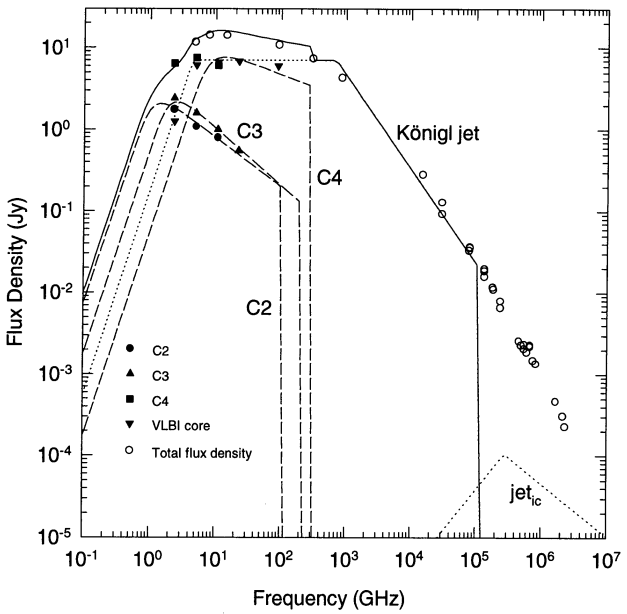

FIG. 11.—Composite spectrum of the VLBI features in 3C 345 near epoch 1982.0 (BMC86). For the superluminal components C2, C3, and C4, spectra were derived by fitting homogeneous sphere models to the VLBI data (*dashed lines*); the Königl jet (see text) was used to model the spectrum of the VLBI core (*dotted line*). Also shown are lines representing the sum flux density of all components (*solid line*) and the inverse Compton spectrum of the Königl jet (labeled "jet$_{ic}$"). Total flux density data are from Bregman et al. (1986; *open circles*). Note that, above the high-frequency cutoff of C4, the Königl jet is the only contributor to the total flux density.

ancy with our value is their use of $\xi = 0.6$ mas for the diameter, whereas we use 0.97 mas. These differences are discussed in BMC86. Stronger limits on θ and γ can be found by combining β_{app} (col. [7] of Table 5) and δ_{min} (col. [9]; cf. Unwin & Wehrle 1992). For C3, these give $\theta_{max,IC} = 14°.1$, $\gamma_{min,IC} = 6.1$, for $h = 1$ (cols. [10] and [11]). In this calculation, we make the assumption that the fluid and pattern speed of the jet are equal. The jet and the combined model give even tighter limits, as shown below.

5.2. *The Conical Jet*

We now model the core (component D) as a circular conical jet of half-angle $\phi = 13°.0 \sin \theta_j$, where θ_j is the angle of the cone axis to the line of sight. (BMC86 give the observed opening angle as 13°.5, but a reanalysis yields 13°.0.) The cone is filled with a plasma moving relativistically with Lorentz factor γ_i, and containing a tangled magnetic field, $B = B_1 r^{-m}$, where r is the distance from the apex and B_1 is the magnetic flux density at $r = 1$ pc (Königl 1981). In a comoving coordinate system the electrons have energy spectrum $N(\gamma)d\gamma = K(r)\gamma^{-p}d\gamma$, where $p = 1 - 2\alpha_0$ is the local injection index, assumed constant along the jet, α_0 is the local spectral index, and $K(r) = K_1 r^{-n}$. We assume that the low-energy cutoff, γ_{lo}, is constant along the jet (with $\gamma_{lo} = 20$); thus the particle density itself varies as r^{-n}. We see the region where this smooth jet has optical depth $\tau \approx 1$ as component D, the "core." Components C4, C3, and C2 are localized regions of enhanced emission at larger distances from the core and lie beyond the region of applicability of the Königl model.

To apply this model, we first have to determine several parameters, the most important of which are α_0, m, and n: these completely specify the spectral slopes in different regimes of the overall spectrum, and we explore this parameter space to find values which yield acceptable fits to the observed slopes. In addition there are several break frequencies which we estimate by analyzing the overall spectrum from the radio to IR. From these spectral slopes and breaks we obtain the theoretical spectrum, which is compared with the observed spectrum in Figure 11. The observed total-flux data are taken from Bregman et al. (1986) and describe the overall spectrum in 1983.3 (near the epoch for which we construct the component radio spectra, 1982.0) except that a correction has been applied to the three lowest frequency points to eliminate the flux from all components except the core.

In the radio the most important parameters are the high-frequency turnover of the synchrotron-emitting jet ($\nu_{sM} = 700$ GHz and $S_{sM} = 7$ Jy), and the spectral index $\alpha_{s1} = 0$ below this turnover. Above the turnover, we set $\alpha_{s2} = -1.15$ to match the IR-optical spectrum, though this is in fact an upper limit since we do not seek to explain the optical emission by synchrotron radiation. In the X-ray regime, the spectral slope is α_{c2}, whose measured value is -0.43 (Worrall & Wilkes 1990).

We choose $\alpha_0 = -0.65$, $m = 1.0$, and $n = 2.0$. The resulting synchrotron-emitting jet spectrum is shown in Figure 11, labeled "jet." The fit of the Königl model plus spheres shows that our choice of parameters is self-consistent; it is not unique, but it is accurate enough for the X-ray calculations, and kinematic parameters derived from them, to be valid. This particular selection of the pair m, n is appealing because it gives a constant flux of relativistic particles if there is continuous reacceleration with fixed upper and lower cutoffs, and it maintains a constant ratio between magnetic and kinetic energy along the jet (Blandford & Königl 1979).

There is only one major discrepancy between model and observation: the best-choice parameter set yields $\alpha_{c2} = -1.2$, much steeper than observed. This is acceptable *if* we also require that the model underpredict the flux density in the X-ray regime; by implication, then, the bulk of the X-ray emission from the core is not inverse Compton from a Königl jet, but must be due to a different process which yields a substantially flatter spectrum. There is weak evidence for a spectral

TABLE 5

SYNCHROTRON SELF-COMPTON MODEL FOR SPHERICAL COMPONENTS FOR EPOCH 1982.0

Component (1)	ν_m (GHz) (2)	S_m (Jy) (3)	α (4)	ρ (mas) (5)	ξ (mas) (6)	$\beta_{app} h$ (c) (7)	$S_{X,IC}\,\delta^{4-2\alpha}$ (Jy at 1 keV) (8)	δ_{min} (9)	$\theta_{max,IC}$ (10)	$\gamma_{min,IC}$ (11)
C2	1.5	2.0	−0.6	4.9	2.15 ± 0.18	8.4	3.2×10^{-5}	2.1	12°.8	8.5
C3	2.6	2.1	−0.7	2.2	0.97 ± 0.07	6.0	6.8×10^{-4}	3.6	14.1	6.1
C4	14.6	7.6	−0.3	0.40	0.29[a] ± 0.02	4.0	1.4×10^{-1}	14.3	2.1	7.7

NOTES.—Limits in cols. (10) and (11) are derived from combining the measured superluminal speeds (col. [7]) with the lower limit to the Doppler factor derived from the synchroton self-Compton calculation (col. [9]) and assuming $h = 1$.

[a] Value for 1983.5.

break which would indicate the presence of two components: $\alpha \sim -0.9$ below 0.5 keV, and $\alpha \sim -0.4$ above 0.5 keV (Unwin et al. 1994).

The final step in the model calculation is to solve for the remaining free parameters of the jet θ_j and γ_j. We apply the constraint $S_{X,IC} \leq S_{Xobs}$, which we do for all β_{app} by varying θ_j until $S_{X,IC} = S_{Xobs}$. The results are shown in Figure 12, which shows the relations among the observable beaming parameters δ_j and $\beta_{app,j}$, and derived parameters γ_j and θ_j (U83). The curved diagonal lines represent the loci of points for which $S_{X,IC} = S_{Xobs}$. These lines are analogous to the vertical line δ = const obtained in the equivalent calculation for a sphere, but, unlike spheres, the jet parameters are aspect dependent and so depend on h. Allowed solutions lie to the right of the diagonal line; how far to the right depends on how weak the actual inverse Compton emission is relative to the total flux. We show results for two different values of h, 1 and 0.5.

Note that the diagonal line defines a maximum value of θ_j for the jet ($\theta_{j,max} = 5.^\circ4$ and $4.^\circ6$ for $h = 1$ and 0.5, respectively); there are no solutions for smaller angles. This is a tighter, more interesting limit than for the spheres. Similarly, there are corresponding lower limits $\gamma_{j,\,min} = 8.0$ and 10.0. These points are shown as stars in Figure 12.

5.3. *Combined Model*

We now construct a model which includes all four components, by combining the geometric constraints provided by the jet and the spheres. We showed in § 4.2.1 that individual components follow curved paths in three dimensions, and the combined model similarly has a curved jet. In § 3.2.2 we showed that β_{app} increases monotonically with radius. The curvature and the apparent acceleration could be caused by changes in θ alone, or γ could be changing also. But, for the reasons discussed in § 4.2.1, we now adopt a constant-γ combined model to represent both the jet and the spheres.

Since β_{app} appears to increase with distance from the nucleus (Fig. 6*b*), we estimated $\beta_{app} = 3.5\ h^{-1}$ for the nucleus, slightly smaller than that for the closest moving component, C4. Here we use $h = 1$; the modification to other values of the Hubble constant are obvious. The Königl model uses the fluid speed,

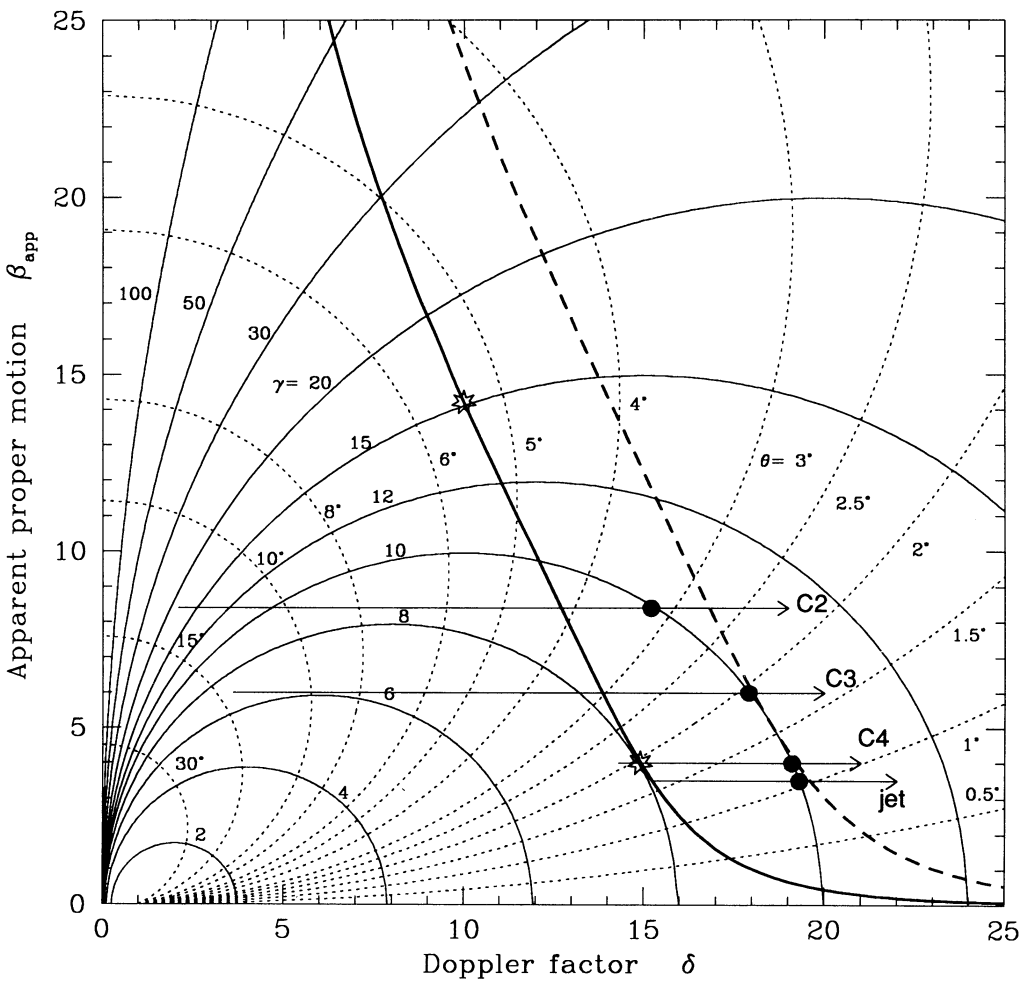

FIG. 12.—Loci of constant Lorentz factor γ and angle to the line of sight θ are shown as functions of the observables δ and β_{app}. A straight, nonaccelerating jet corresponds to a point in this plane, the "operating point." A curved or accelerating jet is represented by a trajectory in this plane. Diagonal lines show solutions for the Königl jet model for $h = 1$ (*solid line*) *and* $h = 0.5$ (*dashed line*); allowed operating points lie to the right of this line. Stars represent limiting values of γ and θ for the jet, for $h = 1$ (*solid line*) and $h = 0.5$ (*dashed line*); allowed operating points lie to the right of this line. Stars represent limiting values of γ and θ for the jet, for $h = 1$. For each of the spherical components C2, C3, and C4, we have a measured β_{app} and a lower limit for δ; these limits are shown as horizontal arrows. Also shown is the line $\beta_{app} = 3.5$ that applies to the jet. The combined model (for $h = 1$) is represented by the solid dots along the curve $\gamma = 10$ (see text).

not the pattern speed we measure from superluminal motion, but for this discussion we assume they are equal. In Figure 12, the line $\beta_{app} = 3.5$ shows the allowed values of δ for the jet.

Next, we selected a value $\gamma_c = 10$ for the combined model, close to the smallest value consistent with all the available kinematic constraints. Then our known values for β_{app} immediately lead to solutions for θ_c. These are shown as dots in Figure 12. Having fixed the operating points, we must check that the limits to the Doppler factor are met (col. [9] of Table 5). The operating points for C2 and C3 lie well to the right of their respective limits, which implies that they contribute little to the observed X-ray flux. However, C4 and D are closer to their limits, and each contributes about a third of the X-ray flux at 1 keV. Thus, in this model, the radio sources produce a substantial fraction of the 1 keV X-rays, by the inverse Compton process. At higher energies the inverse Compton contribution rapidly becomes smaller, because the observed spectrum is much harder than the calculated one. The rest of the X-rays must come from some other process.

This combined model, in which $\gamma_c = 10$ and θ_c increases from $\approx 1°$ to $\approx 3°$ with radius, completely specifies the source geometry. The opening angle of the cone is uncomfortably small: $\phi = 13\overset{\circ}{.}0 \sin \theta_c = 0\overset{\circ}{.}24$ for $\theta_c = 1\overset{\circ}{.}0$ (Fig. 12). This could be ameliorated if the model were relaxed, to allow the pattern speed to be less than the fluid speed (Vermeulen & Cohen 1994).

In correspondence to the small value for ϕ we calculate small values for transverse sizes of the core measured at radii corresponding to 22, 11, and 5 GHz: 0.05, 0.11, and 0.23 mas, respectively. Although these values are well below the resolution limit of the observations, measurable values of diameter were found: 0.3, 1.0, and 2.1 mas, respectively. This is mainly due to uncertainties in measuring such small sizes, as calibration or mapping errors always tend to broaden an intrinsically small source. In addition, some blending of the core with newly emerging components is likely to occur but impossible to account for reliably (BMC86). However, if better maps continue to show such large diameters for the core, then a more elaborate model will be needed, perhaps one involving a cocoon around the jet as an additional source of inverse Compton emission.

Our conclusions are not strongly affected by the choice of Hubble constant. If h is decreased from 1.0 to 0.5, then the values of β_{app} are doubled. We need $\gamma \geq 17$ to accommodate $\beta_{app} = 16.8$ for C2, and the combined model with $\gamma = 17$ gives $\theta \leq 0\overset{\circ}{.}85$. We also tested the sensitivity to ν_{sM}, S_M, β_{app}, and S_{Xobs} by letting them vary by 25% from their nominal values. In general, the most sensitive parameter is ν_{sM}. Its 25% variation gives limiting values of θ (for the combined model) from about $0\overset{\circ}{.}8$ to $1\overset{\circ}{.}5$.

The Königl theory predicts a shift in the location of the core D as a function of frequency because the jet is inhomogeneous and the $r = 1$ region moves closer to the cone apex with increasing frequency ($r_M \propto \nu^{-k_m}$). If the locations of the centroid of the outer components are independent of frequency, as expected if our assumption of homogeneity is valid, this position shift for D translates into the differential shifts shown in Table 6. The spread in row 1 represents a $\pm 25\%$ range in ν_{sM}. Rows 2 and 3 are taken from BMC86 (Table 3). The observed value for the separation between C4 and D refers to 1983.5, during the postacceleration phase. The good agreement in Table 6 is probably fortuitous, but the sign and rough magnitude are correct, and we regard this relation as evidence in favor of the Königl (1981) model, or variants of it (e.g., Hutter & Mufson 1988). We note that our observations are hard to interpret on this point, as especially at the lower frequencies the observed core is typically blended with inner components, i.e., C4 and C5. The calculated shift is insensitive to the input model parameters, and we estimate it is accurate to 15%. Unwin et al. (1994) found the same relation (also in 3C 345) and derived an estimate of k_m to use as an additional constraint on the jet model.

TABLE 6

SHIFT IN COMPONENT POSITION WITH FREQUENCY

Shift	ρ_5–ρ_{11} (mas)	ρ_{11}–ρ_{22} (mas)
Calculated[a]	0.22–0.25	0.10–0.11
Observed:[b]		
C3–D	0.30 ± 0.04	...
C4–D	...	0.11 ± 0.01

[a] Calculated position shift (see text).

[b] Shift in C3–D distance is measured reliably only between 5 and 11 GHz; shift in C4–D distance measured only between 11 and 22 GHz.

5.3.1. *Energetics*

The combined model, since it specifies the jet kinematics completely, enables us to derive various physical parameters, e.g., magnetic field, electron density, and the total pressure; normally these quantities can only be crudely estimated because they depend on δ. The solid lines in Figure 13 show these quantities for the jet for $h = 1$, and the dotted lines are their extrapolations to the radius for C2. If we add the data for the moving components we find that the points for the density and pressure for C3 and C2 fall well below the straight lines, i.e., that the enhanced moving regions of emission have less electron density than the smooth underlying jet. This seems unreasonable, and to remedy it we now choose $f < 1$ (however, we also note that the estimates for the spheres are strong functions of the turnover frequencies and sizes which carry large uncertainties). We pick values of f which raise n_e to the dotted line; this also raises the pressure and lowers the magnetic field. The values we choose, which give the points in Figure 13, are $f = 0.96$, 0.71, and 0.30 for C4, C3, and C2, respectively. (We still use $f = 1$ in the core.) In plotting the points we added 42.8 pc (the value of r at 11 GHz) to the distance calcuated from ρ in Table 5, to get the distance from the apex of the cone. Note that C4 is close to the 5 GHz region of the undisturbed jet. This implies that the smooth Königl model for the jet is not applicable for frequencies much below 5 GHz.

We calculated the pressure by assuming that the electrons are neutralized by protons which have 100 times the energy density of the electrons. Celotti & Fabian (1993), with calculations similar to ours, conclude that the jets should be heavy, i.e., contain protons. They also suggest that the low-energy cutoff of the electron distribution should be about $\gamma_{lo} = 100$, but we use $\gamma_{lo} = 20$ and $\gamma_{hi} = 2000$. Both are needed because the spectral indices are both bigger and smaller than 0.5. The cutoff γ_{lo} is restricted by the need to avoid internal Faraday rotation (Wardle 1977), and γ_{hi} must be sufficiently large to produce synchrotron radiation in the infrared.

The filling factors we chose ($f = 0.3$–1) are arbitrary, apart from bringing the densities up to the extrapolated jet values. We note, however, that they are consistent with high dynamic range imaging, especially of the outer structure (Unwin &

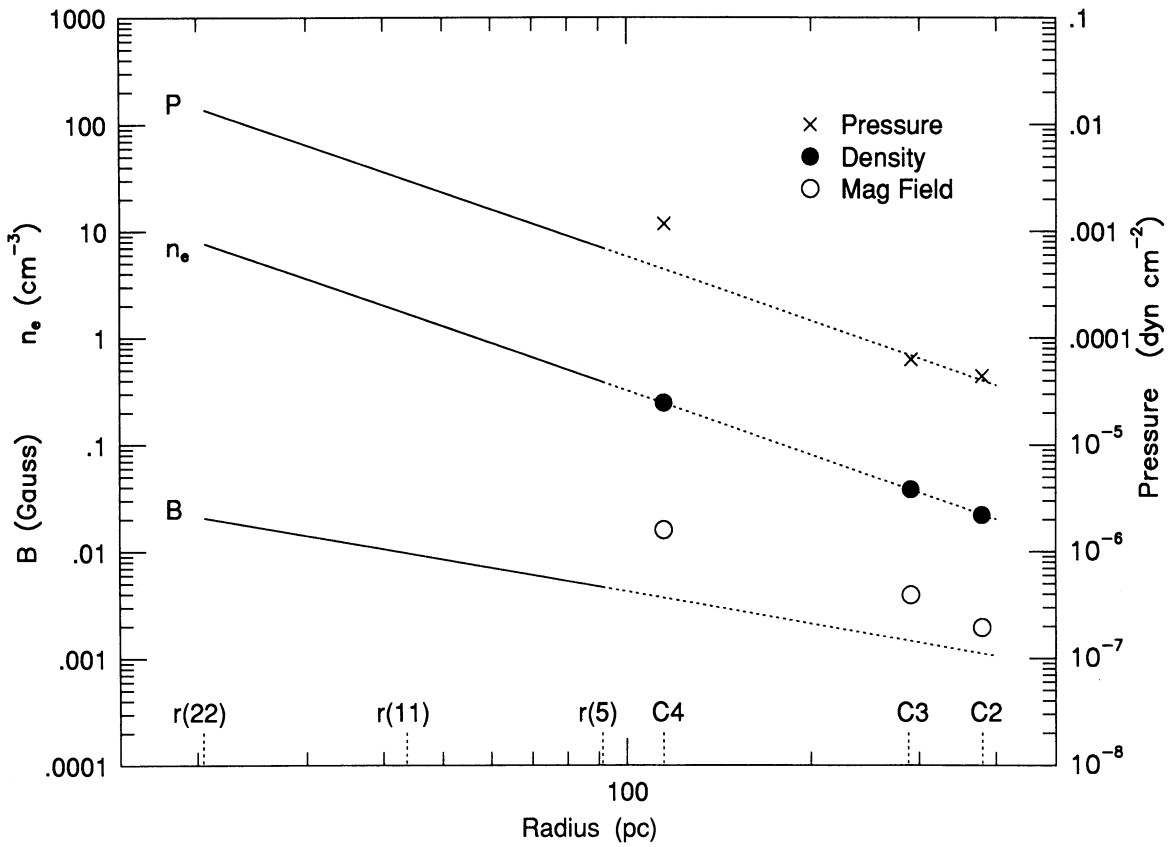

FIG. 13.—Combined model of the jet and the three spherical components C4, C3, and C2, for epoch 1982.0, assuming $h = 1$. For the spheres, plotted symbols represent: total pressure due to electrons, protons and magnetic field (*crosses*), electron density (*solid dots*), and magnetic field (*open circles*). Solid lines show the assumed dependencies of the pressure, electron density, and magnetic field in the jet, with radius ($\propto r^{-2}$, r^{-2}, and r^{-1} respectively). Radii at which 5, 11, and 22 GHz radiation locally dominate the jet emission are indicated on the abscissa. An extrapolation of these lines to the larger radii at which the superluminal components are directly imaged is shown dotted. Note that a filling factor less than 1 is required, to put the component values on or near the dotted lines (see text).

Wehrle 1992). With this choice the ratio of particle energy to magnetic energy is 100–800. We could have chosen smaller filling factors, to make both the density and magnetic field bigger than the extrapolated jet values, but that would have taken us farther from equipartition. These high ratios of particle to magnetic field energy are commonly found in synchrotron calculations of compact sources (Celotti & Fabian 1993).

The pressure in the jet and components is four to six orders of magnitude higher than that in the neighboring narrow-line region (Osterbrock 1988). Thus there is a large pressure gradient at the jet boundary which is perhaps balanced by an azimuthal magnetic field. This pressure imbalance is a common problem of jet models (Blandford 1990).

The kinetic luminosity, obtained by integrating across the Königl jet using the combined model, is $L_{\rm kin} \approx 4 \times 10^{46}\ h^{-2}$ ergs s^{-1} (O'Dea 1984). The observed (radio through IR) electromagnetic luminosity in a comoving frame is $L^*_{\rm obs} \approx 1.6 \times 10^{47}\ h^{-2}\ (\Omega/4\pi)(1+z)^4$ ergs s^{-1}, where Ω is the solid angle of the radiation cone (Bregman et al. 1986). Our beam radius is approximately γ^{-1} (since $\phi < \gamma^{-1}$), which yields $\Omega/4\pi \approx 2.5 \times 10^{-3}\ h^2$ and $L_{\rm kin}/L^*_{\rm obs} \approx 15$.

Celotti & Fabian (1993) estimate the kinetic power in the VLBI jets, and the radiative luminosity of the jet $L_{\rm rad}$, by using a simple combination of VLBI and X-ray measurements. They find, for core-dominated quasars, that $L_{\rm kin}/L_{\rm rad}$ ranges from about 1 to 10^7, and our value of 15 is in their range although below the median. Also, our estimate for the kinetic luminosity, 10^{47} ergs s^{-1} (for $h = 0.5$), is at the top of the range of the quantity Q calculated by Rawlings & Saunders (1991), as an estimate of mechanical power needed to provide the radio power from the lobes of FR II quasars with $z < 1$. It thus appears that 3C 345 is a normal core-dominated quasar. The radiation efficiency of its jet is small, and there is sufficient kinetic luminosity to power the outer radio halo.

Note that the kinetic luminosity depends strongly on our inclusion of protons in the beam. If we had assumed an $e^{\pm}$ beam, then the luminosity would have been $\sim$100 times smaller and the beam would have been only marginally able to power the arcsecond-scale jet and outer halo. We interpret this as evidence in favor of a heavy beam, although of course the specific value of 100 for the proton/electron energy ratio is arbitrary.

6. SUMMARY AND CONCLUSIONS

This work has yielded significant results on the kinematic and spectral properties of the parsec-scale jet in the quasar 3C 345.

1. The image sequences in this study enable us to follow the time evolution of the parsec-scale jet in 3C 345 in considerable detail. In addition to distinct superluminal features, the 5 GHz images indicate emission from an underlying jet. Recent high dynamic range imaging (Unwin & Wehrle 1992) confirms that, beyond a radius of $\approx$3 mas from the nucleus, mostly filamen-

tary extended structure is seen. There also appears to be a trend in our images toward the jet features becoming ill defined with time. At higher frequencies, components persist from epoch to epoch and account for most of the emitted flux density. Our analysis is based on the evolution of these features.

2. The superluminal features move along projected trajectories which are strongly curved near the nucleus, but which straighten at larger radii. Within radius $\rho \approx 2$ mas, the trajectories of components C4 and C5 are distinctly different, and substantial projected bending occurs. The differences in trajectories are less pronounced at larger distances from the core, and C3 and C2 follow similar trajectories.

3. Polynomial fits to the component positions on the sky as a function of time, $x(t)$ and $y(t)$, provide a useful way of combining the imaging results at different frequencies in a form suitable for comparison with jet models. These fits to four superluminal features repesent the best observational data on the time evolution of a relativistic jet and will be valuable in constraining physical jet models.

4. For each superluminal component, the polynomial fits show that the apparent speed increases continuously with distance from the nucleus, with total range of $\sim(3\text{–}10)\, h^{-1}\, c$. We find a relation between the speed and radius from the core which is approximately the same for each component. The fact that a given component does not have a unique speed is important for statistical studies that typically assume a fixed speed for a superluminal feature (Vermeulen & Cohen 1994).

5. The three-dimensional structure of the jet can be reconstructed from the analysis of the trajectories. We show that a curved jet with a constant Lorentz factor ($\gamma = 10$) can explain both the apparent acceleration of components and their modest decline in (Doppler-boosted) flux density with radius. In this model, the intrinsic jet curvature is very slight, but it is greatly amplified by projection effects: the angle of the jet to the line of sight increases smoothly with radius from the core from $\theta \simeq 1°$ to $\simeq 4°$. This model yields less bending at larger distances from the core, which is hard to reconcile with the simplest form of the helical-jet model.

6. Multifrequency monitoring of the total flux density of 3C 345 reveals a broadband flux outburst starting in about 1980 and ending in about 1988. Comparison with our VLBI images shows that these variations are dominated by component C4. More detailed studies of component evolution and spectra and polarization VLBI observations are needed to test models involving shocks (Rabaça & Zensus 1994) and alternatives like the "two-fluid" model (Pelletier & Roland 1989; Lobanov & Zensus 1994).

7. The X-ray emission from 3C 345 can be explained as inverse Compton scattering of radio photons in the parsec-scale radio components. We show that a combined model, based on (1) the Königl inhomogeneous jet model for the radio core and (2) homogeneous spheres for the superluminal components, can explain the jet kinematics, the component radio spectra (including the flat spectrum of the core), and the X-ray flux density and spectrum. This model makes a number of simplifying assumptions and has many free parameters, but we regard its success in explaining very diverse observational data to be significant. The most surprising result is that the best-fit model requires a very small intrinsic opening angle ($\simeq 0.°5$) for the portion of the jet near the apex of the cone which represents the flat-spectrum radio core; the *apparent* opening angle ($\simeq 26°$) is much larger, due to projection effects.

8. Our inverse Compton calculations show that the core and its nearest neighbor (C4 in 1982) dominate the X-ray emission. Similar calculations for earlier and later epochs (C3 in 1980 and C5 in 1989; Unwin et al. 1994; respectively) confirm this result and lead to the tentative conclusion that there exists a characteristic size of $\sim 5\ h^{-1}$ pc for the emission region responsible for (~ 1 keV) X-rays, though it is entirely possible that higher energy X-rays (and any gamma-rays) originate at much smaller radii.

9. The Königl jet model accounts for not only the flat-spectrum core radio emission and observed X-ray flux, but also for the continuum emission from the nucleus of 3C 345 in the millimeter through IR spectral region. No additional contribution to the continuum from dust needs to be invoked (cf. Bregman 1994).

10. With a proton/electron energy ratio of 100, the radiation efficiency of the parsec-scale jet is small, and there is sufficient kinetic luminosity to power the outer radio halo. However, for an electron/positron jet, the kinetic luminosity is barely sufficient, which we take as evidence in favor of a heavy (i.e., proton-dominated) jet.

11. Limits to θ and γ may be deduced from the combined model, which uses both kinematic data from the superluminal features in the jet and constraints from X-ray data. The model argues for a small angle to the line of sight for the core region, $\theta \approx 1°$ for $h = 1$ and smaller still for $h = 0.5$. This constraint can be relaxed if the pattern speed is smaller than the fluid speed, especially for component C4. The most robust limits are $\theta \leq 5.°4$ and $\gamma \geq 8$ ($h = 1$), or $\theta \leq 4.°4$ and $\gamma \geq 10$ ($h = 0.5$).

We acknowledge the contributions to the data analysis by C. Rabaça, A. Lobanov, M. Hodges, P. Barthel, C. Schwarz, E. Gates, and C. Tinney. We thank T. Pearson, T. Krichbaum, and A. Witzel for their comments and suggestions, and J. Wardle for a discussion at the Ringberg workshop on jets in 1992 on the use of polynomials for the description of component motion. E. Valtaoja and H. Teräsranta (Metsähovi Observatory) and M. Aller and H. Aller (University of Michigan) provided results from their monitoring programs. These observations were made possible through the support of the participating observatories of the US and European VLBI Networks, and the JPL/Caltech and Haystack Observatory VLBI Correlators. At Caltech, this work was supported in part by the National Science Foundation under grant AST 91-17100.

REFERENCES

Aller, H. D., Aller, M. F., Latimer, G. E., & Hodge, P. E. 1985, ApJS, 59, 513
Bååth, L. B., et al. 1992, A&A, 257, 31
Band, D. L., & Grindley, J. E. 1986), ApJ, 308, 576
Bartel, N., Herring, T. A., Ratner, M. I., Shapiro, I. I., & Corey, B. E. 1986, Nature 319, 733
Begelman, M. C., Blandford, R. D., & Rees, M. J. 1984, Rev. Mod. Phys., 56, 255
Biretta, J. A. 1985, Ph.D. thesis, Caltech
Biretta, J. A., Moore, R. L., & Cohen, M. H. 1986, ApJ, 308, 93 (BMC86)
Blandford, R. D. 1987, in Superluminal Radio Sources, ed. J. A. Zensus & T. J. Pearson (Cambridge: Cambridge Univ. Press), 310
———. 1990, in Active Galactic Nuclei, ed. T. J.-L. Courvoisier & M. Mayor (Saas-Fe Adv. Course 20) (Berlin: Springer), 230
Blandford, R. D., & Königl, A. 1979, ApJ, 232, 34
Bregman, J. N. 1994, in Multi-Wavelength Continuum Emission of AGN, ed. T. J.-L. Courvoisier & A. Blecha (Dordrecht: Kluwer), 5
Bregman, J. N., et al. 1986, ApJ, 301, 708
Browne, I. W. A., et al. 1982, Nature, 299, 788

Camenzind, M. 1986, A&A, 156, 136
———. 1993, in Lecture Notes in Physics, 421, Jets in Extragalactic Radio Sources, ed. H.-J. Röser & K. Meisenheimer (Heidelberg: Springer), 109
Celotti, A., & Fabian, A. C. 1993, MNRAS, 264, 228
Clark, B. G. 1973, Proc. IEEE, 61, 1242
Cohen, M. H. 1985, in Extragalactic Energetic Sources, ed. V. K. Kapahi (Bangalore: Indian Acad. Sci.), 1
Cohen, M. H., Unwin, S. C., Pearson, T. J., Seielstad, G. A., Simon, R. S., Linfield, R. P., & Walker, R. C. 1983, ApJ, 269, L1
Conway, J. E., & Murphy, D. W. 1993, ApJ, 411, 89
Ghisellini, G., Maraschi, L., & Treves, A. 1985, A&A, 146, 204
Hardee, P. E. 1987, ApJ, 318, 78
Hughes, P. A., Aller, H. D., & Aller, M. F. 1989, ApJ, 341, 68
Hutter, D. L., & Mufson, S. L. 1988, ApJ, 301, 50
Impey, C. G., & Neugebauer, G. 1988, AJ, 95, 307
Jones, T. W., O'Dell, S. L., & Stein, W. A. 1974, ApJ, 188, 353
Kollgaard, R. I., Wardle, J. F. C., & Roberts, D. H. 1989, AJ, 97, 1550
Königl, A. 1981, ApJ, 243, 700
Krichbaum, T. P., & Witzel, A. 1992, Variability of Blazars, ed. E. Valtaoja & M. Valtonen (Cambridge: Cambridge University Press), 205
Ku, W. H.-M., Helfand, D. J., & Lucy, L. B. 1980, Nature, 288, 323
Lobanov, A. P., & Zensus, J. A. 1994, in Compact Extragalactic Radio Sources, ed. J. A. Zensus & K. I. Kellermann (Green Bank: NRAO), 157
Makino, F. 1989, in AGN and the X-ray Background, Proc. 23d ESLAB Symp., ed. J. Hunt & Battrich (Noordwijk: ESA), 803
Maraschi, L., Ghisellini, G., & Celotti, A. 1992, in Testing the AGN Paradigm, ed. S. S. Holt, S. G. Neff, & C. M. Urry (New York: AIP), 439
Marscher, A. P. 1977, AJ, 82, 781
———. 1983, AJ, 264, 296
———. 1987, in Superluminal Radio Sources, ed. J. A. Zensus & T. J. Pearson (Cambridge: Cambridge Univ. Press), 280
———. 1990, in Parsec-Scale Radio Jets, ed. J. A. Zensus & T. J. Pearson (Cambridge: Cambridge Univ. Press), 236
Marscher, A. P., & Gear, W. K. 1985, ApJ, 298, 114
Matveyenko, L. I., Graham, D. A., Pauliny-Toth, I. I. K., Sherwood, W. A., Bååth, L. B., & Kus, A. 1992, Soviet Astron. Lett., 18, 931
Moore, R. L., Readhead, A. C. S., & Bååth, L. 1983, Nature, 306, 44
Moore, R. L., & Stockman, H. S. 1984, ApJ, 279, 465
Murphy, D. W., Browne, I. W., & Perley, R. A. 1993, MNRAS, 264, 298
O'Dea, C. 1984, in NRAO Workshop 9: Physics of Energy Transport in Extragalactic Radio Sources, ed. A. H. Bridle & J. A. Eilek (Green Bank: NRAO), 64
Osterbrock, D. 1988, Astrophysics of Gaseous Nebulae & Active Galactic Nuclei (Mill Valley: University Science)
Pearson, T. J. 1991, BAAS, 23, 991
Pearson, T. J., & Readhead, A. C. S. 1984, ARA&A, 22, 97
Pearson, T. J., & Zensus, J. A. 1987, in Superluminal Radio Sources, ed. J. A. Zensus & T. J. Pearson (Cambridge: Cambridge Univ Press), 1
Pelletier, G., & Roland, J. 1989, A&A, 224, 24
Qian, Shan-jie, Witzel, A., Krichbaum, T., Quirrenbach, A., Hummel, C. A., & Zensus, J. A. 1991, Acta Astron. Sinica, 32, 369
———. 1992, Transl. Chinese Astron. & Astrophys., 16, 37
Rabaça, C. R., & Zensus, J. A. 1994, in Compact Extragalactic Radio Sources, ed. J. A. Zensus & K. I. Kellermann (Green Bank: NRAO), 163
Rantakyrö, F. T., Bååth, L. B., Pauliny-Toth, I. I. K., Matveyenko, L. I., & Unwin, S. C. 1992, A&A, 259, 8
Rawlings, S., & Saunders, R. 1991, Nature, 349, 138
Roberts, D. H., & Wardle, J. F. C. 1994, in Compact Extragalactic Radio Sources, ed. J. A. Zensus & K. I. Kellermann (Green Bank: NRAO), 201
Rogers, A. E. E., et al. 1993, Science, 219, 51
Schilizzi, R. T., & de Bruyn, A. G. 1983, Nature, 303, 26
Schwab, F. R., & Cotton, W. D. 1983, AJ, 88, 688
Shepherd, M. C., Pearson, T. J., & Taylor, G. B. 1994, BAAS, 26, 987
Steffen, W., Zensus, J. A., Krichbaum, T. P., Witzel, A., & Qian, S. J. 1995, A&A, submitted
Tang, G., Bartel, N., Ratner, M. I., Shapiro, I. I., Bååth, L. B., & Rönnäng, B. 1990, in Parsec-Scale Radio Jets, ed. J. A. Zensus & T. J. Pearson (Cambridge: Cambridge Univ. Press), 32
Teräsranta, H., et al. 1992, A&A, 94, 121
Unwin, S. C., Cohen, M. H., Pearson, T. J., Seielstad, G. A., Simon, R. S., Linfield, R. P., & Walker, R. C. 1983, ApJ, 271, 536 (U83)
Unwin, S. C., & Wehrle, A. E. 1992, ApJ, 398, 74
Unwin, S. C., Wehrle, A. E., Urry, C. M., Gilmore, D. M., Barton, E. J., Kjerulf, B. C., Zensus, J. A., & Rabaça, C. R. 1994, ApJ, 432, 103
Valtaoja, E., Teräsranta, H., Urpo, S., Nesterov, N. S., Lainela, M., & Valtonen, M. 1992, A&A, 254, 71
Vermeulen, R. C., & Cohen, M. H. 1994, ApJ, 430, 467
Walker, R. C. 1989, in Synthesis Imaging in Radio Astronomy, ed. R. A. Perley, F. R. Schwab, & A. H. Bridle (San Francisco: ASP), 355
Wardle, J. F. C. 1977, Nature, 269, 563
Wardle, J. F. C., Cawthorne, T. V., Roberts, D. H., & Brown, L. F. 1994, ApJ, 437, 122
Worrall, D. M., & Wilkes, B. J. 1990, ApJ, 360, 396
Zensus, J. A., et al. 1995, in preparation